Lower crustal earthquakes in the East African Rift System: Insights from frictional properties of rock samples from the Malawi rift

Nina Hellebrekers[1], André R. Niemeijer[1], Åke Fagereng[2], Blackwell Manda[3] & Richard L. S. Mvula[4]*

[1] Department of Earth Sciences, HPT laboratory, Utrecht University

[2] School of Earth & Ocean Sciences, Cardiff University, U.K.

[3]Geography and Earth Sciences Department, University of Malawi, Zomba, Malawi

[4]Department of Earth Sciences, Malawi University of Science and Technology, Limbe, Malawi

[*] corresponding author

Abstract

Earthquakes in the southern part of the East African Rift System (EARS) occur at depths up to 45 km in the lower crust, unusually deep for an extensional regime. Typically, earthquakes in continental crust nucleate at temperatures less than 350°C, the temperature at which crystal plastic creep in quartz becomes efficient, corresponding to a depth of ~15 km with an average continental geothermal gradient. Several hypotheses have been proposed to explain the deep seismicity in the EARS, including the presence of high-viscosity mafic material, an abnormally low geotherm, locally elevated strain rates, or high fluid pressures. Here, we provide frictional properties of simulated fault gouges to address the seismic behavior of felsic and mafic crystalline basement rocks from the amagmatic Malawi Rift at the southern, propagating end of the EARS. Rotary shear experiments are conducted at 100, 200, and 250 MPa effective normal stress, a fluid pressure of 100 MPa and from room temperature to 700 °C. The friction of the felsic sample (58% plagioclase) is fairly constant up until 400 °C, after which it decreases. At temperatures of 600 °C and above, the relation between shear stress and effective normal stress deviates from linearity. The friction coefficient of the mafic sample is nearly constant in the considered range of temperature and normal stress and the sample shows a linear relation between normal stress and shear stress. The mafic sample also has negative, and decreasing, *(a-b)* values at temperatures > 400°C. These results are consistent with earthquake nucleation in mafic material, if present, at lower crustal P-T conditions. On the other hand, the data indicate that earthquake nucleation is unlikely in felsic material at temperatures above 500 °C, unless effective normal stress is low and strain rate is elevated by several orders of magnitude.

Introduction

The depth extent of seismogenesis is generally associated with the onset of crystal-plasticity in quartz, which at typical natural strain rates occurs at 300-350 ºC (e.g. Brace & Kohlstedt, 1980, Kirby, 1980). For an average geothermal gradient of 25 to 30 ºC/km, this corresponds to depths of 10-14 km. In the southern East African Rift System (EARS), hypocenters of M6.0 – 7.0 earthquakes have been located much deeper, in the lower continental crust, at 35-45 km depth (e.g Shudofsky et al., 1987; Nyblade & Langston, 1995; Jackson & Blenkinsop, 1997; Foster & Jackson, 1998; Albaric et al., 2009; Yang & Chen, 2010; Craig et al., 2011, Lavayssière et al., 2019). Since the lower continental crust generally behaves viscously (Brace & Kohlstedt, 1980; Kirby, 1980; Scholz, 1988), the crust in the southern EARS must be rheologically different from typical lower crust elsewhere on the continents.

Several explanations have been proposed for a deep seismic-aseismic transition in the EARS. It has been suggested that the depth of the transition is influenced by the presence of old, cold, anhydrous, strong and thick crust and lithosphere (e.g. Shudofsky et al., 1987; Jackson & Blenkinsop, 1993; Nyblade & Langston, 1995; Jackson et al., 2004; Craig et al., 2011). Craig et al. (2011) suggest that thick conductive lithosphere acts as a thermal insulator for the crust from the mantle, which lowers the geotherm, thereby allowing for a larger depth extent of seismogenesis. In order for quartz-rich rocks to generate earthquakes at 35-40 km depth, an average geothermal gradient of 7.5-10 C/km would be

needed. It is also possible that mafic material is present in the EARS lower crust and can account for brittle seismogenic behavior to a deeper level than would be expected for felsic rocks (Shudofsky et al., 1987; Nyblade & Langston, 1995; Albaric et al., 2009; Fagereng, 2013). This is because of the greater viscous strength of mafic rocks (Mackwell et al., 1998). An increased fluid pressure due to the presence of magma or other volatiles could cause local and transient embrittlement within viscous lower crust (Corti et al., 2003), but increased fluid pressures have been considered unlikely in the amagmatic southern EARS where lower crustal earthquakes occur (Craig et al., 2011).

Another mechanism to increase strain rate is by strain localization. The anisotropy of the crust causes weak zones where deformation localizes, increasing the stain rate in these zones (Kirby, 1985). This can allow frictional failure to occur at significantly greater depths than with a homogeneously distributed strain. A condition for these weak zones hosting seismicity at great depths, is that the surrounding rock must be strong and store sufficient elastic strain to generate seismic slip in these weak zones. Fagereng (2013) suggests that seismic behavior at great depths within strong, possibly mafic, lower crust can take place within weak shear zones, where deformation is localized, and strain rate is elevated. This hypothesis agrees with Handy & Brun's (2004) model of earthquakes being signs of transient rheology, and observations of lower crustal pseudotachylytes within mylonites in anhydrous, strong rocks (e.g. Sibson, 1980; Menegon et al., 2017).

Here, we report results from hydrothermal rotary shear experiments on gouges derived from a mafic and a felsic rock from the Malawi rift, an amagmatic segment of the EARS where lower crustal earthquakes have been observed (e.g. Jackson and Blenkinsop, 1993; Nyblade and Langston, 1995; Yang & Chen, 2010; Craig et al., 2011). The samples were tested to analyze trends in friction and friction rate parameters *(a-b)* with temperatures and effective normal stresses going up to 700°C and 250 MPa, respectively. The aim is to obtain frictional properties of the felsic and mafic end member components to identify whether either of the samples could be capable of hosting deep earthquakes. Also, since localization on weak planes may play a crucial role in increasing the strain rate and shifting the brittle-viscous transition deeper, the experimental microstructures were studied to investigate the deformation processes and any evidence for strain localization.

Materials

For these experiments, we selected two end member rock types from the Malawi region, one sample a quartzofeldspathic gneiss (sample M01) and the other a retrogressed, mafic basement gneiss (sample M17). The locations of these samples are indicated in Figure 1. Both samples are crystalline basement rocks with a schistose to gneissic fabric (Figure 2a,b), from high strain zones within outcrops mapped as Paleoproterozoic metamorphic rocks. The mineralogy was analyzed using semi-quantitative XRD as well as by total dissolution in HF and subsequent ICP-MS analysis (Supplementary Table 1).

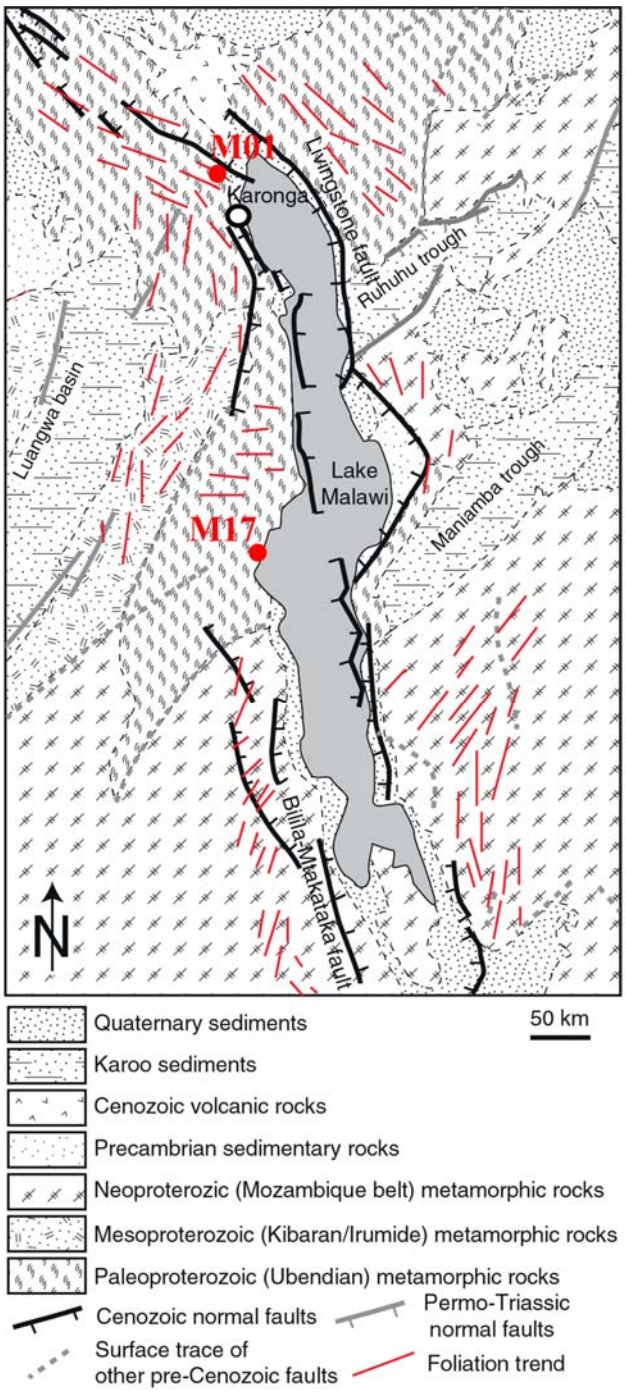

Figure 1: Geologic map showing the sample locations (after Fagereng, 2013).

Table 1: Mineral composition (wt%) of the felsic and mafic sample studied in this research.

M01 (Felsic) Mineral Composition			M17 (Mafic) Mineral Composition	
Mineral	Percentage		Mineral	Percentage
Plagioclase	58%		Hornblende	58%
Muscovite	25%		Oligoclase	13%
Quartz	10%		Quartz	12%
Rest	7%		Ilmenite	4%
			Sphene	3%
			Rest	10%

The relative mineral abundances were calculated on the basis of the minerals identified in the XRD, by optical microscopy, and the whole rock chemistry determined in the ICP-MS analysis and is shown in Table 1.

The felsic sample M01 contains more than 50 % plagioclase with substantial amounts of muscovite and quartz and minor garnet, ilmenite and sphene. It can be classified as a quartzofeldspathic gneiss and was collected adjacent to the Mughese shear zone. The rock contains a well-developed foliation defined by compositional domains (Fig 2a,c), with a superimposed but weakly interconnected micaceous foliation (Fig. 2c). The microstructure is characterized by dynamically recrystallized quartz showing a consistent grain size of tens of micrometers, and a weak shape preferred orientation (Fig. 2c). Feldspar porphyroclasts are present within the pervasively recrystallized quartz matrix, but also have a relatively small grain size which rarely exceeds 100 μm.

Mafic sample M17 consists of hornblende (> 50%) with plagioclase, quartz, and accessory phases. At the outcrop scale, the rock is pervasively lineated and has a foliation defined by feldspar and amphibole rich domains (Fig. 2b). Hornblende crystals show a well-developed shape preferred orientation, also weakly developed in the feldspar layers (Fig. 2d).

Malawi basement rocks are typically Neo-to Paleoproterozoic in age, but the rift valley follows orogenic belts that have been deformed in up to three events at metamorphic grades from amphibolite to granulite (Fig. 1; Versfelt and Rosendahl, 1989). Both samples chosen here contain amphibolite facies minerals, such as hornblende and white mica. They therefore represent rocks that either only reached amphibolite facies temperatures, or that experienced some rehydration subsequent to higher grade metamorphic conditions. Retrograde hydration has long been established as typical of deforming zones in the mid- to lower crust (e.g. White & Knipe, 1978; Wintsch et al., 1995). The rocks are therefore representative of materials that would deform preferentially within granulite facies felsic and mafic gneisses, or of typical felsic and mafic amphibolite facies rocks. There is inevitably variation throughout the Malawi rift around the chosen compositions, but we identify the rocks chosen for the experiments as pervasively sheared (Fig. 2a,b) and likely to have accommodated localized shear strain at mid- to lower crustal conditions. They are therefore suitable for general hypothesis tests on the frictional properties of rocks at mid- to lower crustal conditions in the Malawi rift.

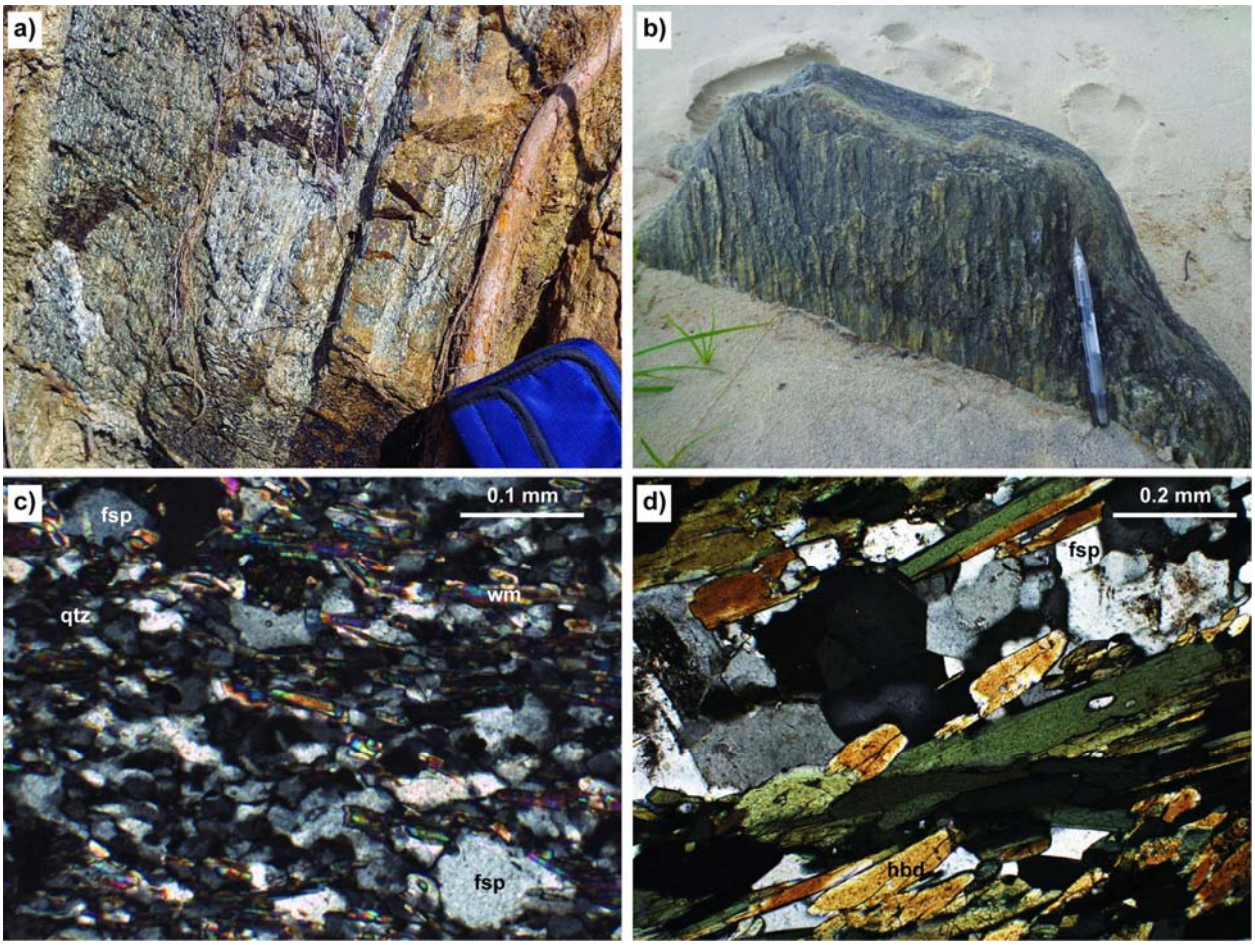

Figure 2:
a) Photo of the outcrop from which sample M01 (felsic) was obtained. See text for description. Compass for scale is ~15x15 cm.
b) Photo of the outcrop from which sample M17 (mafic) was obtained. See text for description. Pen for scale is 15 cm long.
c) Micrograph of a thin section from the hand specimen from which sample M01 was obtained.
d) Micrograph of a thin section from the hand specimen from which sample M17 was obtained

Methods

The samples were crushed with a pestle and mortar and sieved until all particles were smaller than 0.5 mm. This material was subsequently crushed using a Retsch XRD-Mill McCrone to obtain a narrow particle size distribution with an average grain size of 5 μm. Grain size analysis was done with a laser diffraction particle size analyzer. Results can be found in supplementary figure S1.

In order to obtain a reproducible starting layer thickness and porosity, about 0.65 grams of powder with ~0.05 grams of D.I. water was pre-pressed in a dye at a stress of 208 MPa into ring-shaped samples (see also Den Hartog et al., 2012). A hydrothermal ring shear apparatus as described by Niemeijer et al. (2008) and Den Hartog et al. (2012) was used to perform a series of rotary shear experiments (supplementary figures S2 and S3). In these experiments, the ring-shaped sample is sandwiched between two pistons placed inside a pressure vessel. Normal load is then applied to the sample by an Instron loading frame and controlled to within 0.05 MPa. Fluid pressure and temperature inside the vessel can be controlled to within 0.1 MPa and 1°C, respectively. The piston sealing assembly is equipped with a pressure compensation chamber, so that applied fluid pressure does not affect the effective normal stress on the sample. We used demineralized water as the pore fluid which can access the

sample through small gaps between the piston and confining rings. While the top piston is kept stationary, the bottom piston is rotated by a motor in a clockwise direction, creating a dextral shear on the sample. Two load cells in the upper forcing block measure the torque applied to the system by the rotational movement which is then converted into shear stress (resolution of 0.006 MPa for the 1.2 kN loadcells, 0.0249 MPa for the 5 kN loadcell, and 0.0997 MPa for the 20 kN loadcells). Rotary displacement is measured on the base of the vessel using a potentiometer with a resolution of 0.12 μm.

Three types of experiments were done: (1) Constant velocity and constant normal load experiments to create microstructures at selected conditions. In these experiments, the samples were sheared at 1 μm/s for 5000 seconds; (2) velocity stepping experiments at varying temperature; and (3) normal stress stepping experiments at varying temperature (600, 650 and 700°C) and normal stress conditions (50 – 250 MPa), to investigate the dependence of shear stress on effective normal stress, all with a constant pore pressure of 100 MPa. To achieve steady state in these experiments, a run-in was performed at 1 μm/s for 3000 seconds. After this, velocity or normal load was stepped up. The experimental data were inverted to obtain values for *a*, *b*, *(a-b)* and d_c by using an iterative least squares method (e.g. Reinen & Weeks, 1993; Blanpied et al., 1998; Ikari et al., 2009).
The normal load stepping tested the dependence of shear stress on normal stress to establish any divergence from purely linear dependence, indicating deviation from frictional deformation behavior.
The data were acquired at 900 Hz using a 18-bit National Instrument A/D converter and averaged and logged at rates of 1-300 Hz using LabView. Analysis of the data was done using Xlook, in which the data were corrected for the seal friction (normal and shear stress) and the stiffness of the machine (displacement). The apparent friction coefficient of the samples in these experiments was then calculated as $\mu = \tau/\sigma_n^{eff}$, thereby ignoring cohesion. Data were analyzed based on the RSF theory (Dieterich, 1978; Ruina, 1983;), which describes the sliding behavior of a fault with a set of constitutive equations, using the slowness version of the state evolution (e.g. Marone, 1998):

$$\mu_1 = \mu_0 + a \ln\left({V}/{V_0}\right) + b \ln\left({V_0\theta}/{d_c}\right) \quad (1a)$$

$${d\theta}/{dt} = 1 - \left({V\theta}/{d_c}\right) \quad (1b)$$

In these equations, *a* and *b* are material properties for describing friction, in which *a* is seen as the direct effect and *b* as the evolutionary effect. At steady state, the state variable does not change, so equation (1) reduces to

$$(a-b) = {\Delta\mu_{ss}}/{\ln({V_1}/{V_0})} \quad (2)$$

In this equation, $\Delta\mu_{ss}$ is the difference between steady state friction before and after a velocity step, V_0 is the sliding velocity before the step, and V_1 is the sliding velocity after the step.

The velocity dependence of steady state friction, which determines the stability of sliding, results from an interplay between *a* and *b* (e.g. Scholz, 2002). If *(a-b)* > 0, the material is velocity strengthening, which will always lead to stable sliding. If *(a-b)* ≤ 0, a frictional instability can occur at a critical value of effective normal stress ($(\bar{\sigma}_n)_c$). For a given system stiffness, sliding is unstable under quasistatic loading if $\bar{\sigma}_n > (\bar{\sigma}_n)_c$. If $\bar{\sigma}_n < (\bar{\sigma}_n)_c$, it is in the conditionally stable regime, meaning sliding is stable under quasistatic loading, but unstable under dynamic loading if subjected to a jump in velocity exceeding ΔV (Ruina, 1983, Gu et al., 1984, Scholz, 1998).

After the experiment, the samples were dried and impregnated with epoxy resin. The samples were then cut so that the inside of the sample, normal to the shear plane and subparallel to the shear direction, could be studied (Supplementary Figure S4, Verberne et al., 2015).

Results

The evolution of the apparent friction coefficient with displacement at different temperatures and normal stresses is shown in Figure 3 for both samples. All the experiments are characterized by an initial increase in friction which rolls over into a steady level of friction, except for the experiments at 400 and 600 ºC for the mafic sample and at 600 and 700 ºC for the felsic samples. In these cases, an initial increase to peak friction occurs with subsequent weakening, which is larger in the felsic sample. Regardless of temperature, subsequent velocity-steps show the typical response to upward changes in driving velocity; an instantaneous increase in friction followed by a decay towards a new steady state level. At a temperature of 200 ºC (Fig. 3a), unstable slip events or stick slips appear for both samples during the run-in at 1 µm/s and persist during the velocity-steps up to a velocity of 10 µm/s (felsic) or 30 µm/s (mafic) at which point friction stabilizes. At temperatures of 300°C and 400°C (Fig. 3b), strength increases from ~0.6 to ~0.7 for the felsic sample, whereas the friction coefficient for the mafic sample remains relatively stable at ~ 0.7. Some stick slips induced by velocity steps can also be seen for the felsic sample at 300 °C and 400 °C (see Figure 5 for model inversions for two of these steps).

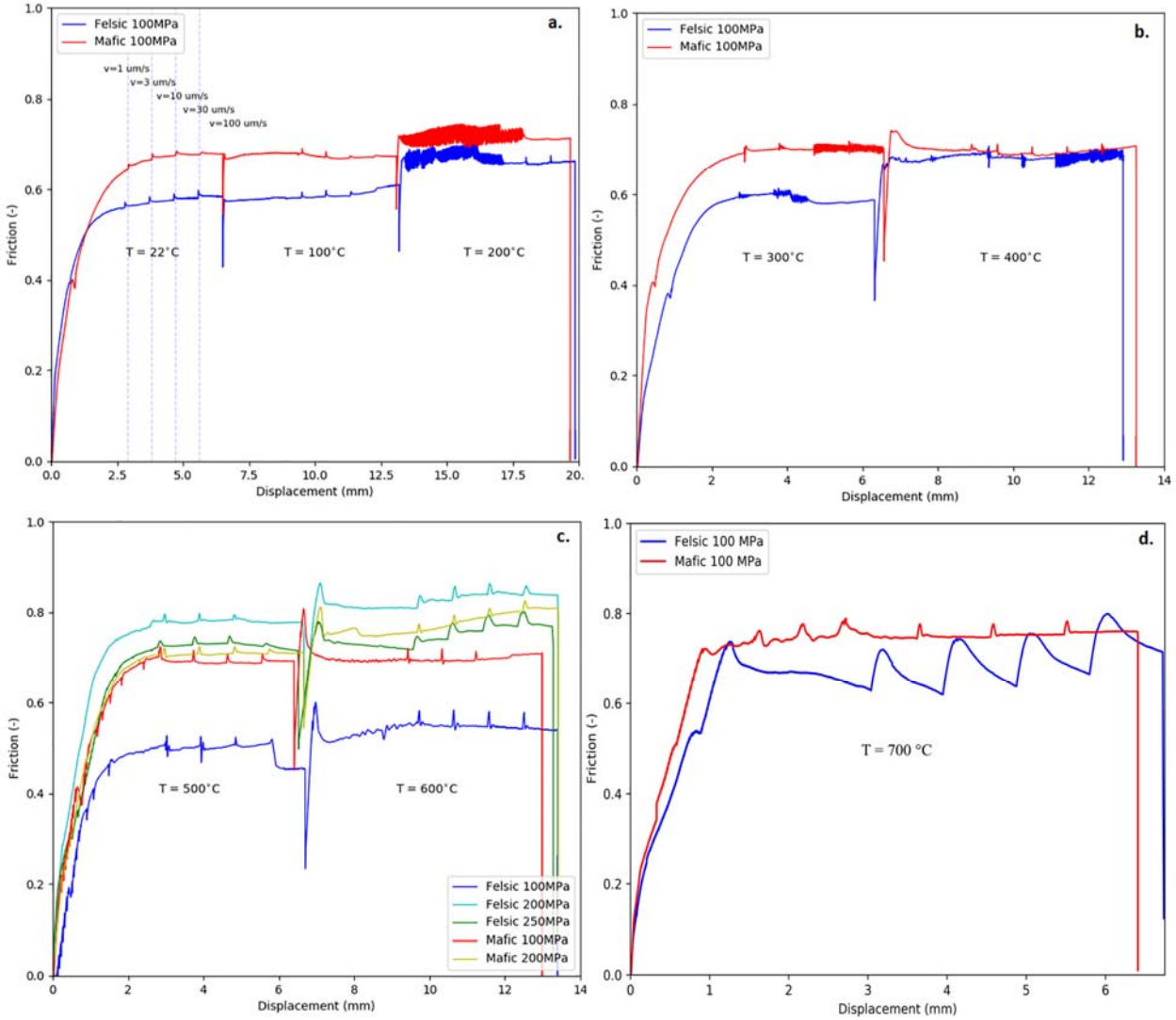

Figure 3: Plots of the evolution of friction with displacement. Temperature and effective normal stress as indicated. Sliding velocity was stepped through the range 1-3-10-30-100 with a displacement for each individual step of 3-0.9-0.9-0.9-0.9 mm, respectively.

Stick slips develop at velocities of 30 µm/s and higher for the mafic sample at 300°C, and at 400°C for the felsic sample. At 500 °C and 600 °C (Figure 3c), the felsic sample at 100 MPa is clearly weaker than at lower temperatures, but the sample has a much higher apparent friction at 200 MPa where it is stronger than the mafic sample. Elevating the effective normal stress to 250 MPa did not increase friction further. The friction coefficient of the mafic sample remains near 0.7 at 500 °C and 600 °C temperatures and 100 and 200 MPa normal stresses. The data for the experiments at 700 °C are shown in Figure 3d. While the mafic sample is again around the same value of friction of ~0.7, the felsic sample shows considerable weakening with displacement, from a peak friction of ~0.55 to 0.45 and subsequently shows strong transient increases in friction as a result of the velocity-steps.

Values of steady state friction for the different samples at different temperatures and normal stresses are presented in Table 2. The steady state friction values were determined after about 3 mm displacement at 1 µm/s. In figure 4, this steady state friction is plotted vs. temperature. At 500 °C and 600 ºC, the values for the mafic sample at 100 MPa and the felsic sample at 250 MPa are very similar. For the mafic sample, the friction coefficient seems to be relatively independent of normal stress and temperature and is around 0.7 for all conditions. The felsic sample has a friction of around 0.55 at low temperatures, then increases to 0.6-0.7 between 200 °C and 400 °C, after which it decreases again. At 200 MPa, apparent friction is considerably higher, up to 0.81 at 600°C.

Figure 6 shows how *(a-b)* values at 100 MPa vary with temperature and velocity. At low (<100 °C) temperatures, *(a-b)* values for both samples are positive, indicating stable sliding behavior. At temperatures larger than 100 °C, *(a-b)* values for both samples are predominantly negative. While the felsic sample has negative *(a-b)* values both for low and high velocities, the mafic sample shows a clear trend with positive *(a-b)* values for high velocities, going towards negative values at low velocities, with the exception of the experiment at 200 °C (Figure 6d). At 700 °C, the felsic sample shows strongly positive *(a-b)* values, that are an order of magnitude larger than typical room temperature values. In comparison, the mafic sample shows a more gradual variation in *(a-b)* values, and still has negative *(a-b)* values at low velocities at 600 ºC. In general, the transitions from negative to positive values for the mafic sample occur at lower velocities with higher temperatures. At constant temperatures of 500 and 600 ºC, higher effective normal stress yields more positive values of *(a-b)*, irrespective of sliding velocity (Figure 7). Values for the individual RSF parameters could not be obtained for all velocity-steps because sliding was frictionally unstable, which makes it impossible for the inversion to find solutions. In these cases, we used the peak friction and the steady state solution (equation 2, see also He et al., 2003) to obtain values for *(a-b)* that are shown in Figures 6 and 7 (see also Tables 3 and 4). Figure 8 shows that the *a*-value shows a mild increase with temperature for the mafic sample, whereas it increases exponentially for the felsic sample at a temperature of > 500 ºC, showing extremely large values of *a* of ~0.1 at a temperature of 700 ºC.

As the felsic sample showed variations in apparent friction with effective normal stress, normal load stepping experiments were performed for this sample. For samples that show purely frictional behavior, shear stress is linearly dependent on normal stress. Figure 9 shows the shear stress (a) and apparent friction (b) as a function of effective normal stress for the felsic sample. At 600°C and 650°C, shear stress at high normal stress is less than predicted by a linear relationship.

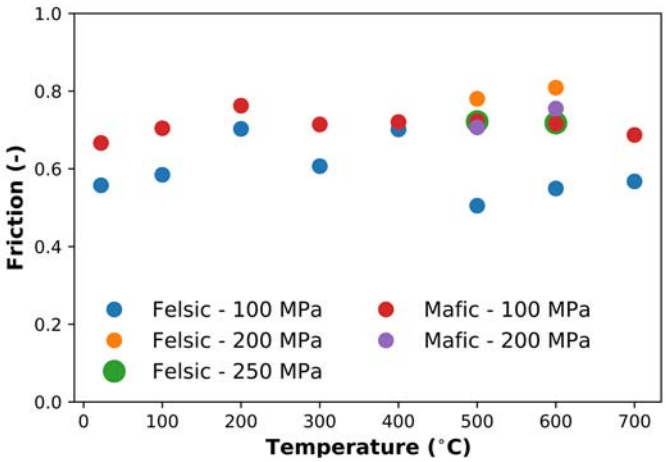

Figure 4: Apparent coefficient of friction (=shear stress / effective normal stress, ignoring cohesion) at the end of the step at 1 µm/s as a function of temperature. Measurement errors are smaller than the symbol size, reproducibility was not tested.

Table 2.

List of experiments and corresponding conditions. Steady state friction at the end of the run-in at 1 mm/s at each temperature is given. The normal stress given is the applied normal stress which is approximately equal to the effective normal stress due to the design of the top block which allows for a compensation of pore fluid pressure (see Niemeijer et al., 2008 for details).

** After this experiment, the piston teeth were deformed and excessive weakening was observed at high normal stress which is most likely related to the deformation of the teeth.*

Exp.	Sample	T (°C)	V(μm/s)	σ_n^{eff} (MPa)	P_f (MPa)	μ_{ss} at 1 μm/s
u556	mafic M17	300-400	1-3-10-30-100	100	100	0.71 – 0.72
u557	mafic M17	500-600	1-3-10-30-100	100	100	0.72 – 0.72
u558	mafic M17	22-100-200	1-3-10-30-100	100	100	0.67 – 0.70 – 0.76
u559	felsic M01	300-400	1-3-10-30-100	100	100	0.61 – 0.70
u560	felsic M01	22-100-200	1-3-10-30-100	100	100	0.56 – 0.58 – 0.71
u561	felsic M01	500-600	1-3-10-30-100	100	100	0.51 – 0.55
u579	mafic M17	500	1	100	100	0.73
u580	felsic M01	500	1	100	100	0.70
u598	mafic M17	500-600	1-3-10-30-100	200	100	0.71 – 0.76
u599	felsic M01	500-600	1-3-10-30-100	200	100	0.78 – 0.81
u608	mafic M17	22	1	100	100	0.72
u609	felsic M01	22	1	100	100	0.56
u610	felsic M01	500-600	1-3-10-30-100	250	100	0.72 – 0.72
u710*	felsic M01	700	1-3-10-30-100	100-125-150-175	100	0.57
u711	felsic M01	600	1	100-125-150-175-200-225-250	100	Figure 9
u712	mafic M17	700	1-3-10-30-100	100	100	0.69
u715	felsic M01	650	1	100-125-150-175-200-225-250	100	Figure 9
u716	felsic M01	700	1	50-75-100-125-150	100	Figure 9

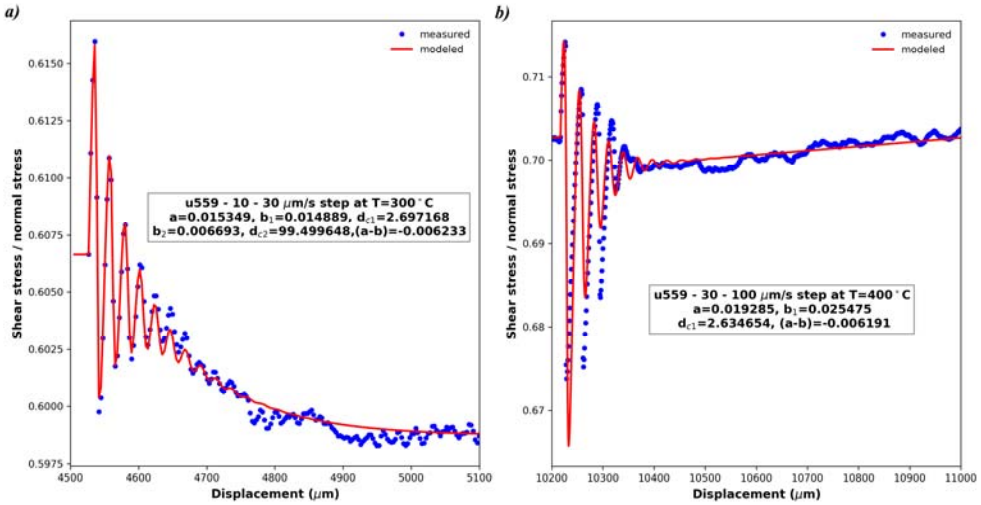

Figure 5: Examples of model fits to the experimental data from experiment u559, which was done on the felsic sample M01 at temperatures of 300 and 400 ºC. The largest standard deviations of the misfits to the models are always on the critical displacement(s) and can be up to 30%, as in the case of the example shown in a), whereas standard deviations on the values of a, b_1 and b_2 are generally less than 1%.

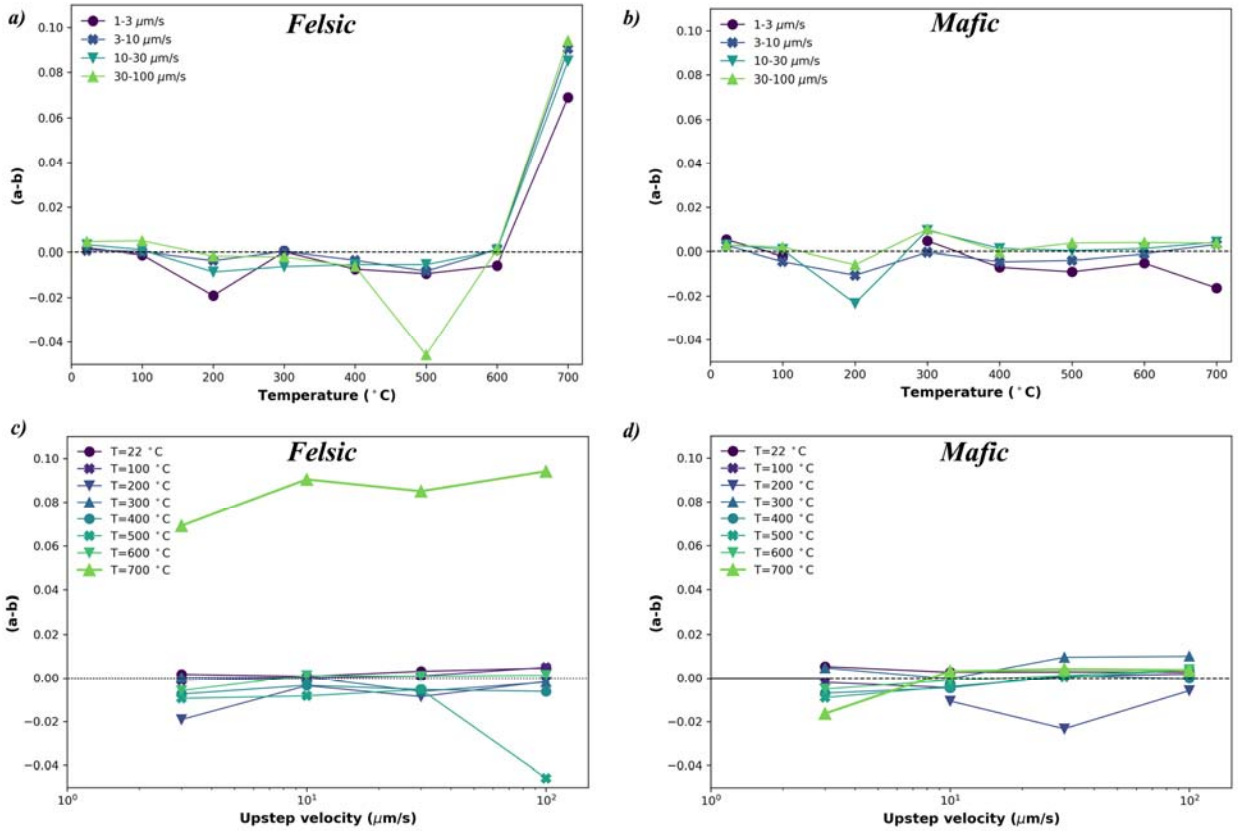

Figure 6:
Plots of (a-b) as a function of temperature (a,b) as well as sliding velocity (c,d) for all experiments performed at 100 MPa effective normal stress (see Tables 2, 3 and 4).
a, c) Felsic sample
b, d) Mafic sample

*Table 3 – Rate-and-state parameters for the mafic sample. Experimental conditions can be found in Table 1. The standard deviations (s.d.) of the fitted parameters are only given for the critical slip distances d_{c1} and d_{c2}. The standard deviations of the other parameters are smaller than 0.1% of the value. The last column displays the linear hardening or weakening trend (linear term, l.t.) which was used to detrend the data of that particular velocity step. Steps denoted with * result in stick-slips or transient stick-slips. Most of these cases could not be modeled and the values are not available (n/a). Values from the manual calculation (see main text) are given where they result in negative values.*

	T ºC	v_0 µm/s	v_1 µm/s	a $x10^{-2}$	b_1 $x10^{-2}$	d_{c1} μm	s.d.	b_2 $x10^{-2}$	d_{c2} μm	s.d.	(a-b) $x10^{-2}$	l. t. $x10^{-6}$
u556	300	1	3	1.6395	1.1673	41.884	0.32	0	0	0	0.4722	5.4
u556	300	3	10	4.017	4.2321	1.0605	0.01	0.1959	3.25	0.41	0.192	0
u556*	300	10	30	1.1557	n/a	n/a	n/a	n/a	n/a	n/a	< 0	n/a
u556*	300	30	100	2.4284	n/a	n/a	n/a	n/a	n/a	n/a	< 0	n/a
u556	400	1	3	2.5314	2.7789	7.2038	0.11	0.4475	59.71	2.71	-0.695	-0.9
u556	400	3	10	3.6922	3.1252	1.9897	0.12	1.017	35.58	2.30	-0.450	8.5
u556	400	30	100	3.2857	2.6268	1.7091	0.06	0.5272	29.62	0.57	0.1317	0
u557	500	1	3	3.6698	3.1438	16.634	0.18	1.428	83.84	0.99	-0.902	0
u557	500	3	10	4.3033	3.3963	5.41	0.15	1.296	50.59	0.66	-0.389	-0.7
u557	500	10	30	3.3081	2.3322	8.103	0.40	0.9403	53.47	1.71	0.0355	-1.0
u557	500	30	100	3.7906	2.5131	2.992	0.12	0.8947	43.05	0.48	0.3827	0
u557	600	1	3	4.6270	4.4992	5.019	0.10	0.6363	42.78	1.40	-0.5085	0.5
u557	600	3	10	6.7742	5.5859	2.719	0.07	1.287	14.69	0.54	-0.0983	5.0
u557	600	10	30	6.0006	4.8424	3.572	0.10	1.029	22.83	1.20	0.1293	5.0
u557	600	30	100	5.6886	4.6598	3.874	0.13	0.6251	43.94	4.00	0.4037	5.0
u558	22	1	3	2.2836	1.4289	1.34	0.05	0.3201	55.12	1.92	0.5345	23.0
u558	22	3	10	1.4701	0.8128	9.217	0.35	0.3798	79.52	2.15	0.2775	7.0
u558	22	10	30	1.5675	0.8297	9.942	0.38	0.4456	84.19	2.07	0.2922	-1.7
u558	22	30	100	2.2662	1.3962	4.501	0.54	0.5836	66.10	2.61	0.2865	-1.5
u558	100	1	3	1.2818	1.0839	7.813	0.12	0.4001	87.39	1.38	-0.2022	-8.0
u558	100	3	10	1.4414	1.2296	6.294	0.10	0.6563	126.9	1.25	-0.4445	3.0
u558	100	10	30	2.1118	1.5439	3.359	0.28	0.4733	41.08	1.98	0.0946	0.9
u558	100	30	100	4.1353	3.4903	1.700	0.05	0.4479	79.78	3.34	0.197	0
u558*	200	1	3	n/a	n/a	n/a	n/a	n/a	n/a	n/a	< 0	n/a
u558*	200	3	10	n/a	n/a	n/a	n/a	n/a	n/a	n/a	-1.0582	n/a
u558*	200	10	30	n/a	n/a	n/a	n/a	n/a	n/a	n/a	-2.3302	n/a
u558	200	30	100	1.2208	1.3167	3.814	0.28	0.4868	86.78	5.47	-0.5828	6.0
u598	500	1	3	4.5324	3.8955	4.599	0.01	1.134	51.33	0.23	-0.4972	8.5
u598	500	3	10	2.7890	2.2538	8.092	0.17	0.856	63.17	0.68	-0.3208	5.3
u598	500	10	30	2.3630	1.3820	10.975	1.31	0.71	45.88	2.94	0.2710	-5.0
u598	500	30	100	1.8281	1.2651	14.08	0.70	0.8469	193.8	3.02	-0.2839	7.0
u598	600	1	3	3.5360	3.1488	9.751	0.10	0.4667	86.53	1.35	-0.0795	17.9
u598	600	3	10	4.0153	2.7716	7.179	0.24	0.9908	18.08	0.21	0.2529	15.6
u598	600	10	30	4.581	3.4601	7.664	0.23	0.7671	38.62	0.70	0.3538	11.4
u598	600	30	100	3.5843	2.7368	16.567	0.22	0.3024	405.6	52.4	0.5452	-0.1
u712	700	1	3	1.6549	0.724	13.866	1.31	2.566	157.5	1.46	-1.635	0.0
u712	700	3	10	4.8514	3.7259	9.0460	0.21	0.8093	79.04	2.27	0.3162	0.0
u712	700	10	30	5.9714	4.4915	6.1434	0.40	1.059	30.09	1.49	0.4212	2.0
u712	700	30	100	4.9649	3.6702	7.9088	0.68	0.9183	37.63	3.09	0.3765	4.0

Table 4 – Rate-and-state parameters for the felsic sample, same as in Table 3.

	T ºC	v_0 µm/s	v_1 µm/s	a $x10^{-2}$	b_1 $x10^{-2}$	d_{c1} μm	sd	b_2 $x10^{-2}$	d_{c2} μm	sd	(a-b) $x10^{-2}$	l. t. $x10^{-6}$
u559*	300	1	3	1.4709	1.5626	1.7935	0.43	-0.128	7.356	9.37	0.0358	7.9
u559*	300	3	10	2.1108	3.3928	2.2121	0.30	-1.327	5.475	0.66	0.0449	0.0
u559	300	10	30	1.5349	1.4889	2.6971	2.12	0.6693	99.49	37.3	-0.6233	-2.0
u559	300	30	100	2.9355	2.7121	1.1987	0.02	0.4169	38.60	1.83	-0.1936	8.3
u559	400	1	3	1.4287	1.4105	1.1211	0.39	0.7559	21.87	2.76	-0.7377	-2.7
u559	400	3	10	1.8026	3.7437	5.0683	0.19	-1.602	25.49	1.95	-0.3389	5.1
u559	400	10	30	1.9747	2.5081	2.2209	0.05	0	0	0	-0.5334	5.3
u559	400	30	100	2.9355	2.7121	1.1987	0.02	0.4169	38.60	1.83	-0.1936	8.3
u560	22	1	3	1.2864	0.7658	13.621	0.20	0.339	71.61	1.10	0.1815	8.7
u560	22	3	10	1.4187	0.8845	11.873	0.20	0.4449	89.52	1.19	0.0892	6.0
u560	22	10	30	1.6425	0.7155	7.54	0.15	0.6046	33.67	0.33	0.3224	1.0
u560	22	30	100	1.8059	0.9714	11.046	0.15	0.3692	55.30	0.86	0.4653	-1.8
u560	100	1	3	1.4771	1.053	9.009	0.15	0.5294	82.60	1.02	-0.1053	5.0
u560	100	3	10	1.7527	1.1699	8.127	0.18	0.5553	57.80	1.01	0.0275	1.5
u560	100	10	30	1.8862	1.2704	9.82	0.31	0.5082	80.31	2.27	0.1075	10.0
u560	100	30	100	2.1178	1.0336	7.518	0.55	0.5836	31.42	1.16	0.5006	9.8
u560*	200	1	3	1.4348	n.a.	n.a.	n.a.	n.a.	n.a.	n.a.	-1.915	0
u560	200	3	10	1.9622	2.3197	2.7217	0.12	0	0	0	-0.3576	0
u560	200	10	30	1.6748	1.7953	3.038	0.02	0.7395	145.4	0.77	-0.86	9.9
u560	200	30	100	2.1345	2.036	3.765	0.03	0.2579	127.3	2.12	-0.1594	5.3
u561	500	1	3	3.4560	4.3926	7.9928	0.04	0	0	0	-0.9365	10
u561	500	3	10	3.2804	4.1077	5.8977	0.07	0	0	0	-0.8274	13
u561	500	10	30	3.1632	3.699	4.5247	0.12	0	0	0	-0.5358	11
u561	500	30	100	4.1797	3.7384	1.4872	0.17	5.024	94.82	1.19	-4.5824	0
u561	600	1	3	5.8549	5.402	6.5672	0.08	1.034	138.2	2.02	-0.5807	0
u561	600	3	10	6.0867	5.9626	9.6216	0.11	0	0	0	0.1241	-3.4
u561	600	10	30	6.3314	5.6436	10.437	0.04	0.5913	97.34	1.02	0.0965	-3.8
u561	600	30	100	7.6335	6.634	5.3615	0.05	0.8628	67.44	0.74	0.1366	-6.1
u599	500	1	3	3.1433	2.9302	9.6491	0.09	0.6964	222.5	3.60	-0.4832	0
u599	500	3	10	3.6036	3.1688	4.9159	0.13	0.657	116.3	1.95	-0.2222	5.2
u599	500	10	30	4.9794	4.4122	3.5629	0.07	0.6146	198.5	10.1	-0.0473	-6.6
u599	500	30	100	2.7861	2.8418	3.1497	0.27	0	0	0	-0.0557	0
u599	600	1	3	3.8352	5.7425	39.445	0.24	-3.479	61.93	0.38	1.5712	0
u599	600	3	10	4.7971	4.1622	17.185	0.20	-0.210	228.1	24.5	0.8446	2.6
u599	600	10	30	4.7782	4.2919	17.847	0.72	-0.243	71.48	19.1	0.7295	-8.2
u599	600	30	100	3.2705	2.9783	32.458	1.14	0	0	0	0.2922	-3.0
u610	500	1	3	5.348	4.5478	5.443	0.01	0.7217	117.3	0.51	0.0785	5.9
u610	500	3	10	2.7522	1.9789	14.426	0.49	0.5769	91.00	2.52	0.1964	-9.2
u610	500	10	30	3.8797	2.938	9.389	0.45	0.7241	84.96	1.96	0.2176	-9.2
u610	500	30	100	4.4076	3.5269	4.209	0.07	0.7319	114.7	2.31	0.1488	-12.0
u610	600	1	3	4.9138	3.482	24.475	0.23	-0.395	160.7	4.45	1.8273	3.5
u610	600	3	10	8.6737	5.2784	7.91	0.2	2.043	58.15	0.74	1.3523	3.0
u610	600	10	30	11.674	8.0181	9.055	0.78	2.057	48.44	3.55	1.5992	-8.0
u610	600	30	100	9.1078	7.4733	16.575	3.06	1.157	184.7	23.5	0.4772	-6.0
u710	700	1	3	12.839	5.9218	51.70	7.40	0	0	0	6.9174	-70
u710	700	3	10	14.395	5.3482	133.54	0.92	0	0	0	9.0477	-100
u710	700	10	30	14.937	6.427	124.17	1.92	0	0	0	8.5108	-73
u710	700	30	100	14.613	5.1941	134.92	2.39	0	0	0	9.419	-69

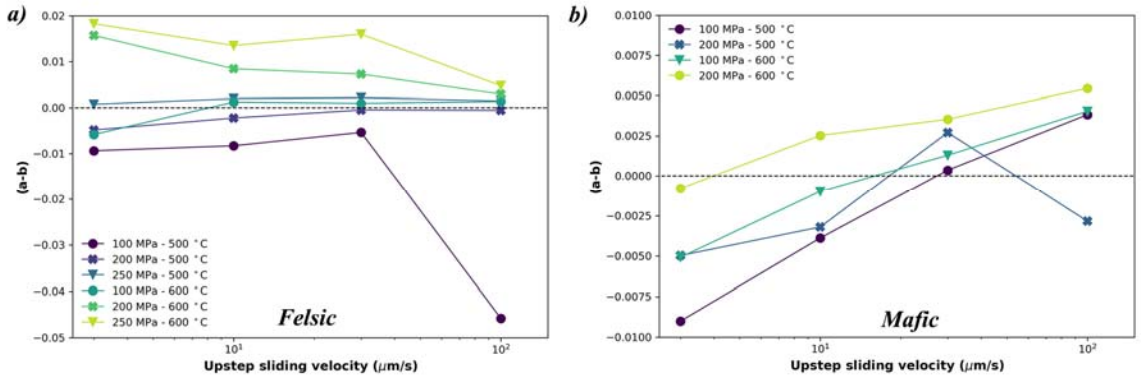

Figure 7:

a) *Plots of (a-b) as a function of sliding velocity for experiments performed at effective normal stresses of 100, 200 and 250 MPa as well as 500 and 600 ºC for the felsic sample*
b) *Plots of (a-b) as a function of sliding velocity for experiments performed at effective normal stresses of 100, 200 and 250 MPa as well as 500 and 600 ºC for the mafic sample*

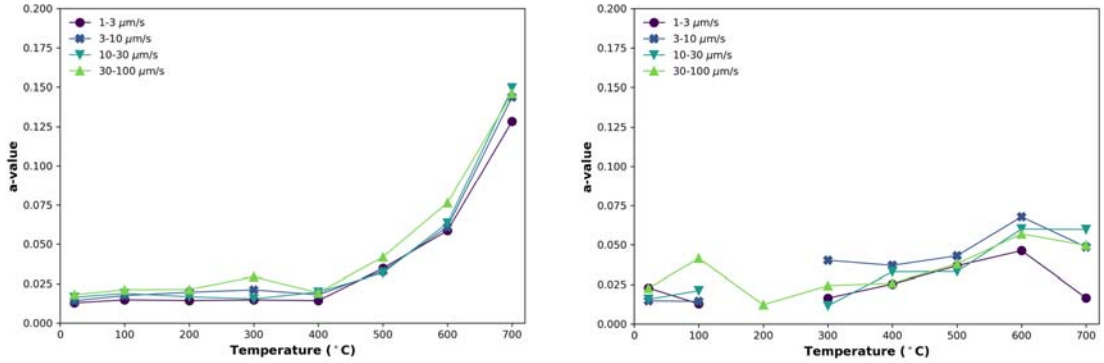

Figure 8:

a) *Plot of the value of a, the direct effect parameter in rate-and-state friction as a function of temperature for the felsic sample.*
b) *Plot of the value of a, the direct effect parameter in rate-and-state friction as a function of temperature for the mafic sample.*

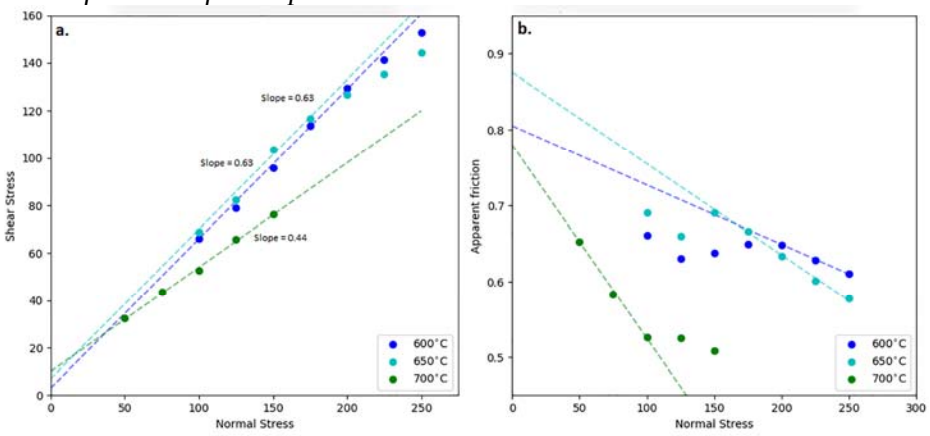

Figure 9:

a) *Plot of shear stress as a function of effective normal stress with linear fits to the data for temperatures of 600, 650 and 700 ºC*
b) *Plot of apparent friction as a function of effective normal stress for temperatures of 600, 650 and 700 ºC*

While the slopes of the linear fits at 600°C and 650°C are the same, the slope at 700 °C is much shallower. Overall, shear stress clearly becomes a more non-linear function of normal stress with increasing normal stress and temperature for the felsic sample.

Microstructural observations

Upon disassembly of the piston pair and removal of the confining rings, almost all samples fragmented into numerous small pieces. Typically, these pieces fracture along inclined and curved planes from the inner side of the annulus to the outer one. This results in a variable thickness of the recovered gouge layers. A notable exception is the sample deformed at a constant velocity of 1 μm/s and 700 °C (u716), of which several pieces were recovered to span the full gouge layer thickness.

In the following, we only discuss the microstructures of the experiments performed at a constant sliding velocity, to avoid the issue of a complicated velocity and temperature history (see Table 2). Note that these experiments were sheared for 5 mm only. The mafic sample sheared at room temperature and a constant velocity of 1 μm/s (Figure 10a) has developed a few subtle shears at low angle to the sample top and base. These shears are recognized from tabular zones of relatively finer grain size (indicated in red). The contrast in grain size is not large and is most obvious by the general absence of larger grains (~10 μm). The amount and length of localized shears increases in the sample deformed at 500˚C (Figure 10b). Here the shears are recognized both as cracks that opened after sample removal from the apparatus, and by locally reduced grain size within thin, tabular zones. These shears lie at an angle of about 15°, clockwise and anti-clockwise, to the base of the sample as expected for R and P shears. There is no clear shape-preferred orientation of grains in either the mafic sample deformed at room temperature, or in the mafic sample deformed at 500˚C. Grains have locally developed intragranular fractures at both room temperature and 500˚C.

A weakly developed, preferred orientation of muscovite can be seen in the felsic sample deformed at room temperature (Figure 11a,c). In the felsic sample sheared at 500 °C, however, a clearer foliation has developed locally (Figure 11b,d,e), dipping to the left in a section cut parallel to the dextral shear direction, as expected for S planes in an S-C configuration. The sample deformed at room temperature also has a weak foliation, but in the opposite direction to that expected for S planes. whereas tabular zones of reduced grain size (indicated in red) dip in both P and R-shear orientations (Figure 11a,c). In both samples, cracks (indicated in blue) have opened in the Riedel orientation as well as in a non-planar horizontal orientation, presumably upon unloading of the sample. These unloading cracks may have opened along either brittle R-shears reflecting grain comminution, or along a well-developed foliation, as they are also in the S orientation (Figure 11d,e). These cracks are more continuous and more frequent in the sample deformed at 500˚C, consistent with the better-developed foliations in this sample.

In the samples deformed in normal stress stepping experiments at temperatures of 600, 650 and 700 °C (Figure 12), a well-developed muscovite preferred orientation is visible in the microstructure, in an S plane orientation (Figure 13). However, this shape-preferred orientation becomes less clear with increasing temperature. The long axes of the muscovite grains in the sample deformed at 700 °C are either horizontal or dipping into an S plane orientation (Figure 13c). All samples have areas of higher density, reflected by lighter color in the backscatter images, what may be interpreted as lower porosity (Figures 12, 13) The grain boundaries in these areas are not sharp and seem somewhat smeared out. These areas cover larger parts of the samples with increasing temperature. Also, some of these areas seem to follow a boundary-parallel or R-shear orientation, particularly at 700 °C.

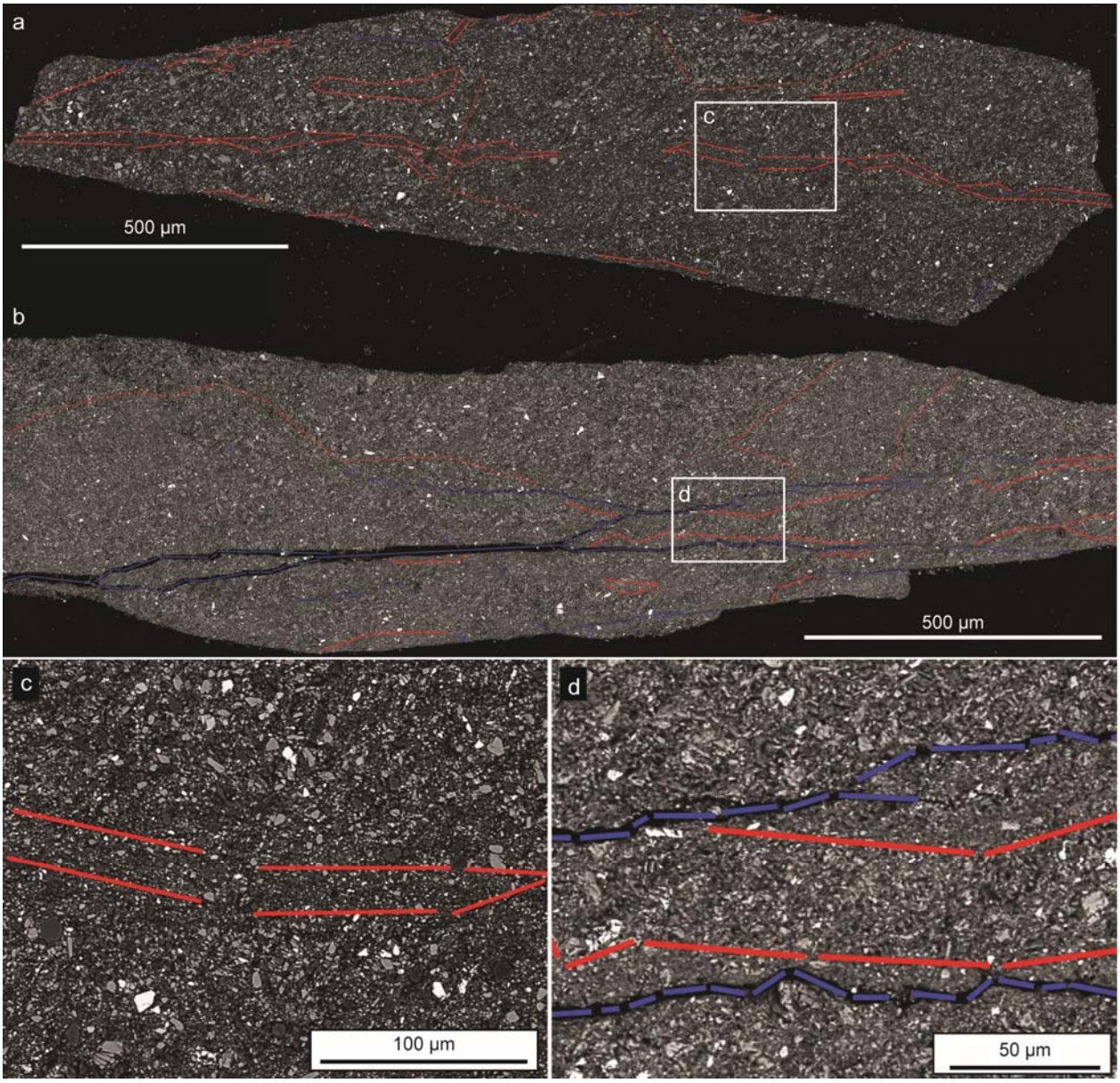

Figure 10:

Overview microstructures of the mafic samples deformed at a constant velocity of 1 µm/s for 5 mm at an effective normal stress of 100 MPa and at (a) room temperature and (b) 500 ºC. Cracks are indicated by blue lines, zones of grain size reduction are indicated by red lines. Sample thickness in both cases is about 800 µm and shear sense is top-to-the-right.

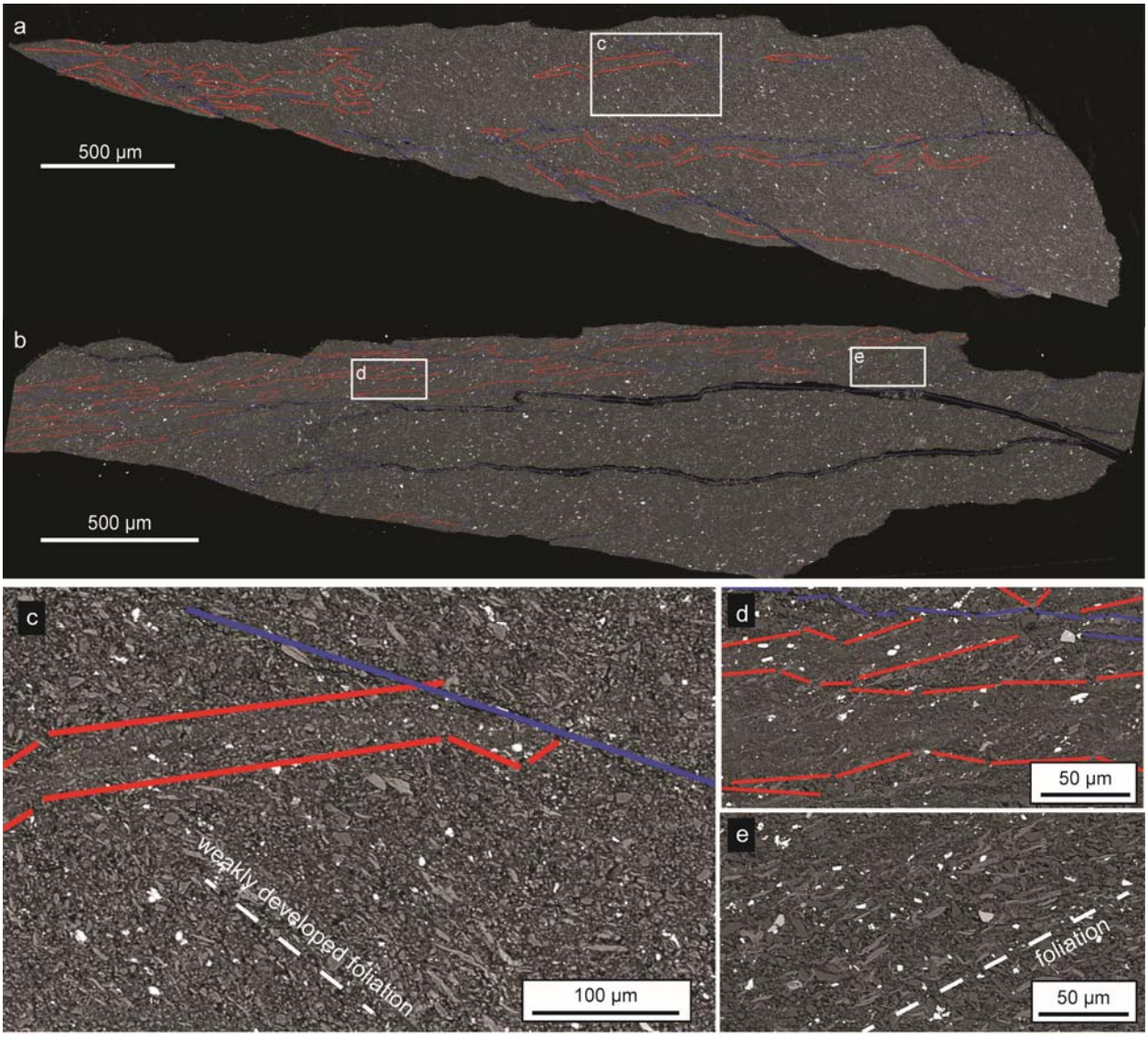

Figure 11:

Overview microstructures of the felsic samples deformed at a constant velocity of 1 µm/s for 5 mm at an effective normal stress of 100 MPa and at (a) room temperature and (b) 500 ºC. Cracks are indicated by blue lines, zones of grain size reduction are indicated by red lines. Sample thickness in both cases is about 800 µm and shear sense is top-to-the right. White boxes indicate the location of the close-ups shown in (c) for the relation between cracks, zones of finer grain size, and poorly developed foliation in the room temperature sample, and in (d) and (e) for the 500˚C sample.

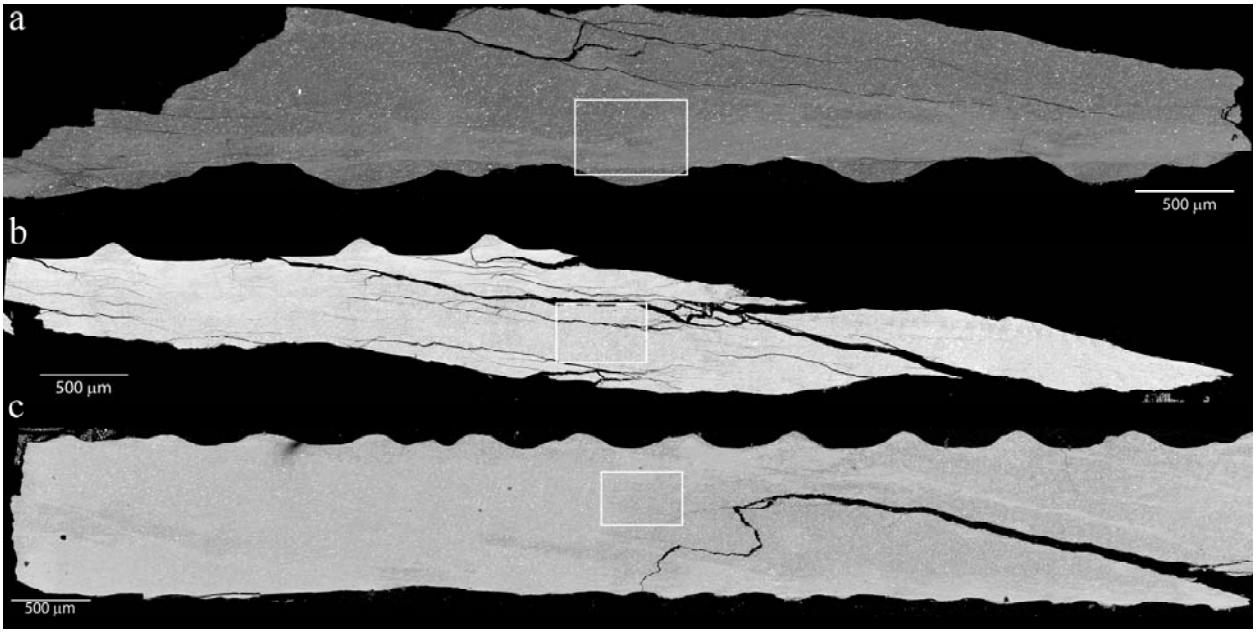

Figure 12:

Microstructures obtained in normal-stress-stepping experiments using the felsic sample at 1 µm/s and temperatures of 600 (a), 650 (b) and 700 ºC (c). A faint foliation defined by aligned muscovite is present and denser zones are visible as lighter areas. These areas appear to increase in size with increasing temperature. White boxes indicate the locations of the close-ups, shown in Figure 13. Shear stress is top-to-the-right in all cases.

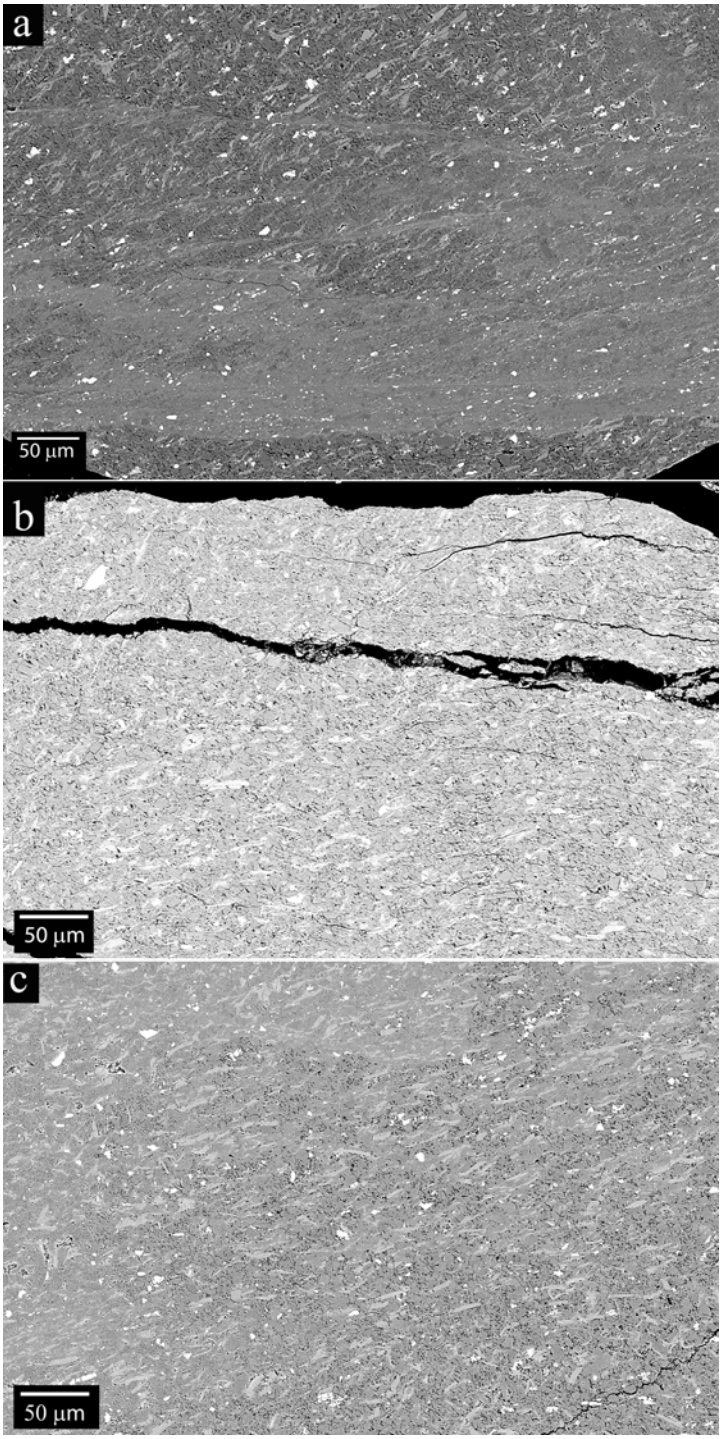

Figure 13:

Details of the microstructures of the felsic sample deformed at 1 µm/s and temperatures of 600 (a), 650 (b) and 700 ºC (c). Shear sense is top-to-the-right in all cases.

Discussion

Frictional Properties of the felsic sample

Our felsic sample is somewhat similar in composition to Rhode Island Westerly granite (where Westerly granite has 30% quartz, 30% microcline, 30% oligoclase and 5-10 % biotite, Tullis and Yund, 1977), but contains less quartz and more muscovite. In general, steady state friction is comparable to experiments on gouges of Westerly granite (e.g. Blanpied et al., 1991, 1995), tested at similar conditions. At less than 400˚C friction at 100 MPa is between 0.55 – 0.6, and increases to 0.7 at 400 °C. At temperatures over 400°C, friction decreases significantly (Figure 4). The results up to a temperature of 400 ºC are comparable to those obtained by He et al. (2013) on wet plagioclase gouges (μ=0.73), but these authors did not observe weakening at temperatures above 400 ºC. A decrease in friction to 0.5 was observed by Blanpied et al. (1995) at 600 ºC and a sliding velocity of 0.1 μm/s, which is comparable to the decrease we observed at an order magnitude faster velocity and at 500 ºC.

The velocity dependence of friction is also similar to that of Westerly granite. The values are positive at a temperature below 100 ºC, then transitions to negative, to return to strongly positive values again at high temperatures. This aseismic-seismic-aseismic pattern has been recognized by many authors (e.g. Chester & Higgs, 1992; Blanpied et al., 1995; Chester, 1995; Den Hartog et al., 2012). Results of pure plagioclase gouge, on the other hand, show only mild variations of the values of *(a-b)* with increasing temperatures, with values showing mildly velocity-weakening behavior with values clustering around -0.005 (He et al., 2013). A particular noteworthy observation of our experiments is the strong increase in the *a*-value with increasing temperature, in particular at 700 ºC (Figure 8). Typically, the direct effect is linked to the inherent rate-dependence of contact strength (e.g. Beeler et al, 2007). Therefore, any significant changes in the value of *a* should be the results of a change in the dominant deformation mechanism. An additional observation is that the shear stress dependence on normal stress begins to deviate from linearity at temperatures of 600 ºC and higher, in particular for high effective normal stress (> 200 MPa), similar to what has been observed for calcite (Verberne et al., 2017) and dry salt with increased confining pressure (Shimamoto, 1986). One possible explanation is that the pore fluid within the sample is no longer drained to the pressure-controlled reservoir due to a strong decrease in porosity, which could cause a decrease in the actual effective normal stress on the sample (Faulkner et al., 2018). However, if this was the case, dilatant hardening would be observed upon doing velocity steps (Faulkner et al., 2018), which we did not observe.

Another possibility is that temperature-dependent variations in frictional properties of the felsic sample are caused by an increase in the contribution of crystal-plastic behavior at temperatures from 600 °C and higher. We can calculate the flow strength of the individual minerals using flow laws of dislocation creep of the type (e.g. Ranalli, 1995):

$$\dot{\varepsilon} = A\sigma^n \exp\left(\frac{-\Delta H}{RT}\right) \quad (4)$$

This equation can easily be rewritten to obtain shear stress (e.g. Niemeijer et al., 2016). Using parameters for quartz or anorthite (Ranalli, 1995), we obtain values that are in the GPa range and are thus far too high to explain the observed weakening and non-linearity in the normal stress dependence. On the other hand, we observe a weak foliation defined by the preferred orientation of muscovite (Figure 11), which should deform much easier by dislocation glide (Shea and Kronenberg, 1992, Mariani et al., 2006) following a flow law of the exponential type according to:

$$\dot{\varepsilon} = \exp(c\sigma)\exp\left(\frac{-\Delta H}{RT}\right) \quad (5)$$

The peak shear stresses after velocity-steps for the experiments at 600 and 700 ºC are shown in figure 14 both in log-log space to derive the stress exponent *n* (as in equation 4) and in log-linear space to obtain the pre-exponential factor *c* (as in equation 5). The fits to the (limited) data show that at 600 ºC and 100 MPa effective normal stress, both equations fit poorly with slopes that are meaningless. In contrast, the data at 700 ºC can be fit with equation (4) with a stress exponent of 23 or alternatively with equation (5) with a pre-exponential factor *c* of 0.41.

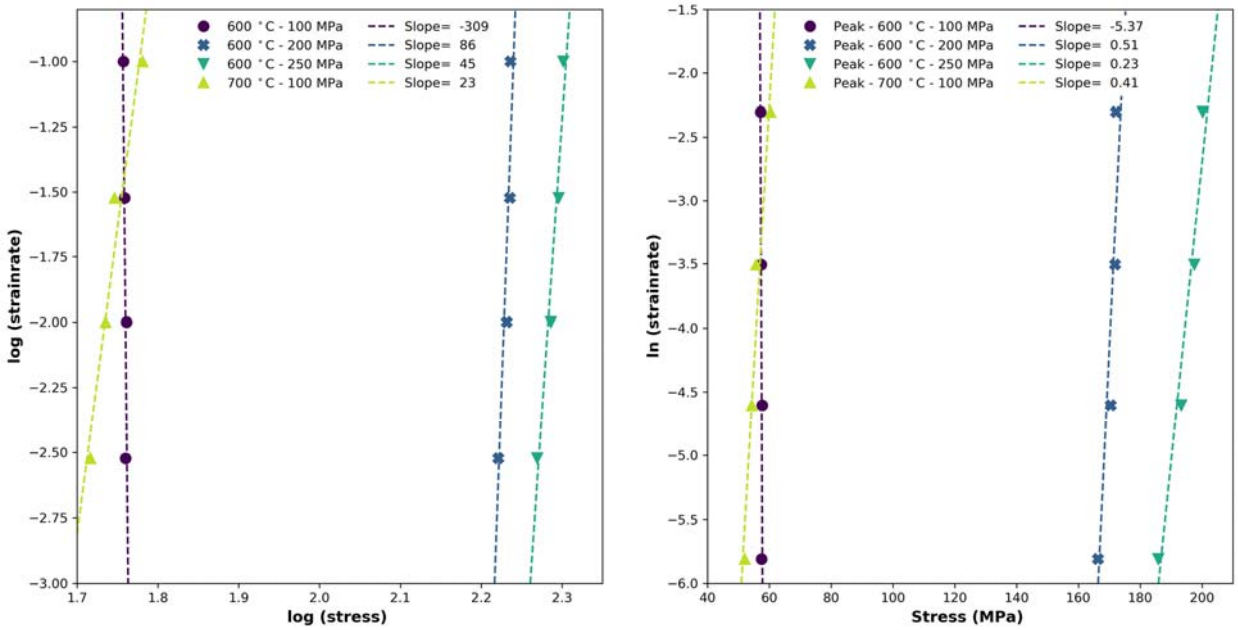

Figure 14:
Plots of the peak shear stress for the three different up-step velocities (3-10-30 µm/s) which have been converted to strain rates by dividing over the gouge layer thickness of 1 mm. a) Plot in log-log space, showing the stress exponent in a power flow law as the slope b) Plot in semi-log space, showing the pre-exponent constant in an exponential flow law as the slope.

This value is in between the values of the two end-member flow laws for muscovite (c=0.15 and c=0.55) obtained by Shea & Kronenberg (1992). We have only a very limited number of data points so this resemblance could be completely fortuitous. At the same time, we observe a weak shape preferred foliation of muscovite so we might speculate that the rapid increase in the a-value is a result of the increased contribution of dislocation glide within muscovite grains.

Frictional properties of the mafic sample

The mafic sample behaves completely differently from the felsic sample at our experimental conditions. It shows a consistent friction coefficient of about 0.7 at all tested temperatures and effective normal stresses. This sample contains mostly hornblende, of which not much is known. Although recognizing that there are likely differences in frictional properties of amphiboles (hornblende) and pyroxenes, as a mafic rock, the results could be compared to gabbro. He et al. (2007) & (2013) find steady state friction values for gabbro of between 0.7 – 0.75 for temperatures between room temperature and 600°C and normal stress up to 300 MPa, which are similar to our results here.

The *(a-b)* values for the mafic sample generally decrease with decreasing velocity, showing more negative values at the lower velocities. The low-velocity *(a-b)* values are still in the unstable regime at temperatures up to the tested 700 °C. The results from the pyroxene gouges from He et al. (2013) show similar *(a-b)* trends. The mafic sample does not show any significant changes in microstructures with temperature, with some zones of fracture development and grain size reduction and without a clear fabric development.

The friction coefficient of the mafic sample is independent of temperature and normal stress and shows linear behavior. This potentially indicates that the controlling deformation mechanism in the mafic sample does not change in the range of temperatures, effective normal stresses, and strain rates tested here. This is likely due to a high viscous strength of mafic material (Mackwell, 1998), meaning that the material is easier to deform brittlely than plastically up to higher temperatures. This interpretation is

consistent with the absence of clear microstructural evidence for plasticity in the mafic sample. Through the entire P-T range tested, it therefore seems to behave by granular or cataclastic flow.

Implications for lower crustal earthquakes

Several explanations have been proposed for deep crustal earthquakes in general, and in the EARS specifically. With their greater viscous strength, mafic rocks can account for a deeper brittle-viscous transition than felsic rocks (Fagereng, 2013; Albaric et al., 2009; Shudofsky et al., 1987; Nyblade & Langston, 1995). Also, the thick, conductive lithosphere will act as a thermal insulator for the crust from the mantle, which lowers the geotherm (Craig et al., 2011), and deepens the brittle-viscous transition. However, even with the coldest thermal structure calculated for the rift environment, temperature at the depth of the lower crustal earthquakes (35-44 km) would still be on the order of 600-700°C (Fagereng, 2013). In our experiments, while the felsic sample behaves as expected of a rock going from dominantly brittle to viscous deformation, deformation behavior in the mafic sample remains exclusively brittle and frictional. The friction parameters found for the mafic sample show that it is in the unstable regime at high temperatures and at lower velocities, indicating that it is capable of generating unstable (earthquake) slip under these laboratory conditions, whereas the felsic sample is firmly in the velocity-strengthening regime. Therefore, the felsic sample, which represents the quartzofeldspathic gneisses that dominate Malawi basement geology (Fig. 1; Bloomfield, 1966; Carter and Bennett, 1973, Chapola and Kaphwiyo, 1992), is likely to accommodate steady creep at depths where lower crustal earthquakes occur in the southern EARS. Of the two samples tested here, the only sample that might be able to host the nucleation of deep earthquakes is the mafic sample. Note that this inference requires an extrapolation over several orders of magnitude in loading velocity or strain rate (Figure 14). Shear zones with mafic components may be a particularly good candidate for lower crustal earthquakes, as has previously been suggested by Brodie and Rutter (1987) based on field observations in the Ivrea Zone of northern Italy.

Nucleation of deep earthquakes in rocks that are represented by our felsic samples is highly unlikely, since we observe strongly velocity-strengthening behavior at the highest temperature tested and at 600 ºC, the sample becomes more velocity-strengthening with increasing effective normal stress. This implies that in order to obtain velocity-weakening behavior, we need an elevated strain rate due to strain localization as well as an elevated pore fluid pressure that decreases effective normal stress (e.g. Sibson, 1980), such as CO_2 that has previously been suggested to modulate seismicity on normal faults (Parry and Bruhn, 1990; Miller et al., 2004). In the Magadi-Natron basin of the Kenya-Tanzania border region, surface CO_2 anomalies have been explained by flow of mantle fluids along major faults that penetrate the lower crust (Lee et al., 2016). However, such examples of potential deep fluid flow in the southern EARS are few, and more data are required to determine whether this is a widespread process. Equally, magmatic activity could potentially trigger seismicity, as it does in the northern EARS. In Tanzania, an early stage of magmatism may be a locally possible explanation for a long-lasting deep earthquake sequence (Albaric et al., 2010). No evidence has, however, been presented for active magmatism south of the Rungwe Volcanic Province in southern Tanzania, and thus it is difficult to invoke magmatic triggers of earthquakes anywhere in Malawi.

One could envisage that a lower crustal high strain zone with mixed felsic-mafic composition could host earthquakes if the distribution and size of mafic and felsic parts allows for propagation of earthquakes through the felsic proportions of the fault (Figure 14). Numerical simulations and linear stability analysis using rate-and-state friction equations with double spring-slider configurations have demonstrated that seismic slip can be hosted on faults that are composed of a mixture of velocity-weakening and velocity-strengthening materials (Skarbek et al, 2012; Luo & Ampuero, 2018). The size and proportion of velocity-weakening patches (i.e. mafic bodies in this case) that are needed to generate a fault-spanning seismic event, depend on the values of $(a-b)$ and d_c of both the velocity weakening and velocity strengthening materials, the effective normal stress within the two materials and the stiffness of the fault. Luo & Ampuero (2018) formulated three terms that control the mode of slip in a heterogeneous fault:

$$\alpha = \frac{(b_w - a_w)\sigma_w}{(a_s - b_s)\sigma_s} \qquad \beta = \frac{L_w(b_w - a_w)\sigma_w}{G d_{cw}} \qquad \xi^2 = \frac{d_{cw}}{d_{cs}} \tag{6}$$

Here, the subscript *w* denotes the property of the velocity-weakening material and *s* is for the velocity-strengthening material and *G* is the shear modulus. In the limiting case of a large β (>1) and a small ξ^2 ($<10^{-1.5}$), there is a value for α above which the fault will rupture in a fault spanning event. This limiting value α_{TC} is proportional to the ratio of fault area of velocity weakening material over velocity-strengthening material, *f*, defined as L_w/L_s. Assuming a high effective normal stress at 40 km depth, we expect β to be much larger than 1. The critical or character slip distance d_{cs} we determined for the felsic material at 700 ºC was on the order of several 100s of µm and about one order of magnitude higher than d_{cw} of the mafic material, considering d_{c1}, fulfilling the requirement of a small ξ^2. Taking the *(a-b)*-values for both materials at 700 ºC and 1 µm/s, we get a value for α of 0.2, which would indicate that *f* is 5, or that fault area taken up by velocity-weakening mafic material has to be 5 times larger than the area with felsic material in order for an earthquake to propagate through the felsic patches. In order to obtain a more accurate estimate of the size of mafic bodies that would be needed for fault-spanning ruptures to occur on mixed felsic-mafic faults, numerical simulations beyond the 2-D simulations of Luo & Ampuero (2018) are needed which is beyond the scope of the present work. Note also that in this simple calculation, we have disregarded any possible velocity-dependence of the rate-and-state friction parameters, in particular of *(a-b)*. A velocity dependence of *(a-b)* is expected when thermally activated, time-dependent mechanisms contribute to the deformation (Chen & Spiers, 2016). For our felsic sample at 700 ºC (Figure 6) or 600 ºC and high normal stress (Figure 7), we observe either no velocity dependence of *(a-b)* or an increasing *(a-b)* with decreasing velocity. We therefore expect that at natural strain rate, the felsic sample is strongly velocity-strengthening, with *(a-b)*-values that are inversely proportional to the stress exponent of the controlling deformation mechanism. On the other hand, particularly our data for the mafic sample at 600 ºC (Figure 7) shows a loglinear decrease in *(a-b)* with sliding velocity. Extrapolating this to the loading rates inferred in the EAR of 2-3 mm/year or 0.1 nm/s, we obtain a value of -0.03 (Figure 15). Our simplified extrapolation without a microphysical model basis still suggests that the proportion of velocity-weakening mafic material must be at least 1.5 times larger than the area of velocity-strengthening material. Here, we implicitly assume that deformation occurs within a 1 mm-thick zone, but the actual slip zone could be thinner in nature. In this case, the strain rate is higher and the difference with the experimental strain rates is thus smaller. To summarize, under natural loading conditions we would expect different *(a-b)*-values than those we obtained at our experimental loading rates. At the same time, what trends we have in our experimental data indicate that the two rock types change behavior in opposite directions: with decreasing velocity, the felsic sample becomes more velocity-strengthening, whereas the mafic sample becomes more velocity-weakening (Figure 15) The calculation indicates, overall, that seismicity on faults embedded in a compositionally heterogeneous, hydrostatically pressurized, lower crust requires the faults to be volumetrically dominated by mafic rocks, at least given the boundary conditions and materials considered in this study.

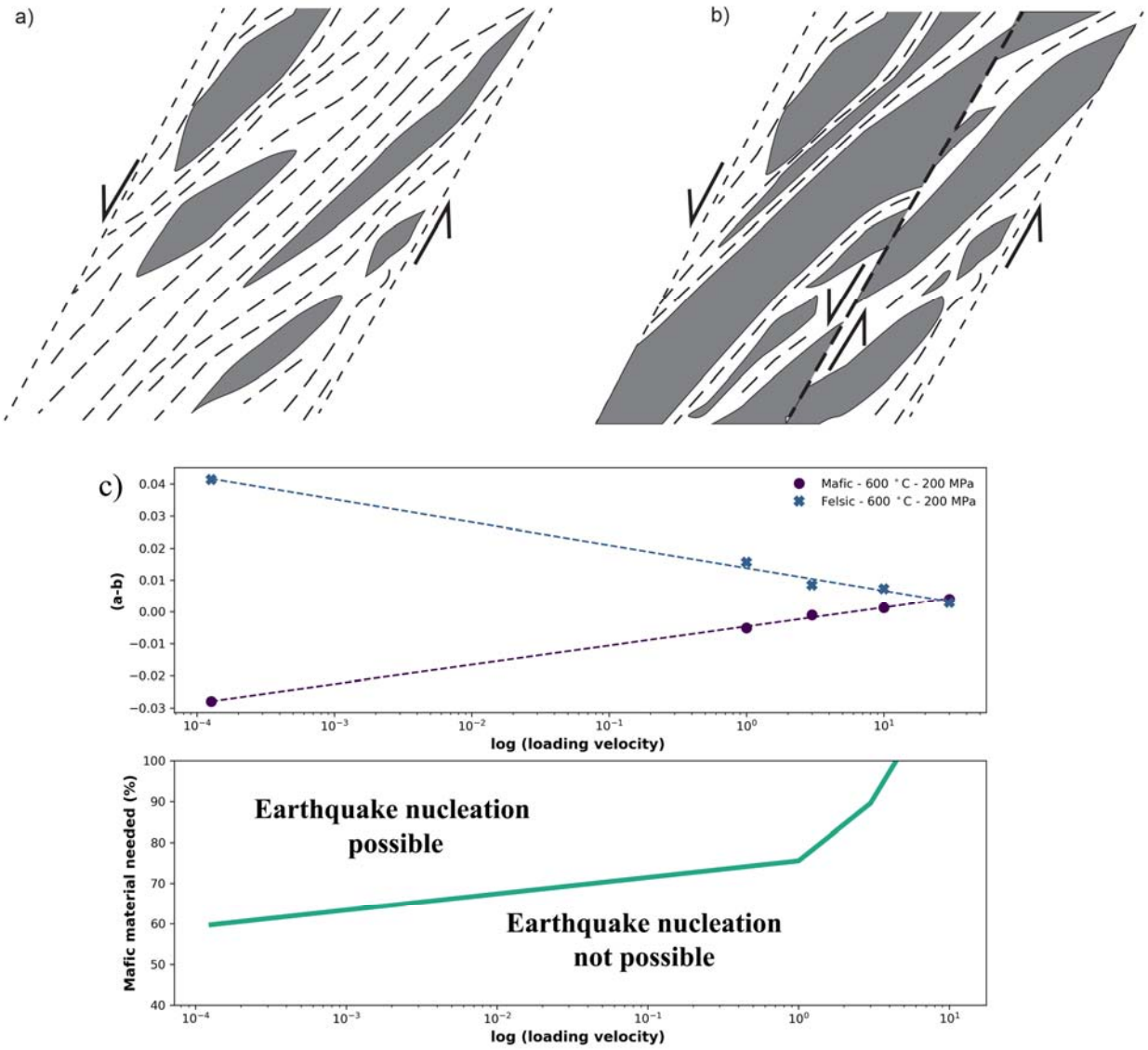

Figure 15:

Schematic of the envisioned fault zone structure at depth, with transposed and dismembered layers of mafic/velocity-weakening material (grey) within a felsic/velocity-strengthening matrix (white with dashed lines denoting foliation). The mafic layers are inferred to have been transposed within a ductile shear zone; the timing of transposition and the original orientation of the layers is not inferred nor implied.
a) Dominantly felsic/ductile/velocity-strengthening, deforming through distributed deformation
b) Contains substantial transposed mafic/velocity-weakening layers, along which a discontinuity (thick dashed line) can form and involve more than 80 % velocity-weakening material.
c) *Log-linear extrapolations of experimental data obtained at 600 ºC and 100 MPa effective normal stress and inferred amount of mafic (velocity-weakening material) needed to nucleate an earthquake that ruptures the entire fault (i.e. that ruptures through the velocity-strengthening felsic material).*

Conclusions

In order to evaluate which rock types are most likely involved in the deep crustal earthquakes (35-45 km) that occur in the southern, amagmatic, East African Rift System, we performed a series of hydrothermal friction experiments on fault gouge prepared from felsic and mafic samples from Malawi. Experiments were done at effective normal stresses of 100 to 250 MPa, a fluid pressure of 100 MPa and temperatures ranging from 20 to 700 °C. To establish the velocity dependence of friction, quantified via the parameter *(a-b)*, sliding velocities were instantaneously stepped in the range of 1 to 100 μm/s in 3 and 3.5-fold steps. We can conclude the following:

1) Apparent friction of the fault gouge derived from the mafic sample is 0.7 and does not show much variation with temperature up to the maximum temperature tested (700 ºC).
2) The apparent friction of fault gouge derived from the relatively feldspar-rich felsic sample increases slightly with temperature from ~0.55 at room temperature to 0.7 at a temperature of 400 °C and decreases at temperatures above that. This behavior is similar to that established for granites.
3) Both samples show frictionally unstable behavior and negative *(a-b)* values over a broad range of temperatures and sliding velocities. The felsic sample, however, becomes strongly velocity-strengthening at temperatures from 600 ºC.
4) Sliding shear strength of the felsic sample shows deviations from a perfect linear dependence on effective normal stress at temperatures of 600 ºC and above.
5) We infer that the onset of ductility of one of the phases in the felsic sample is the cause of both the non-linearity in normal stress dependence and the weakening. The most likely mechanism, at laboratory conditions, is fluid-assisted diffusion creep because an estimate of dislocation creep flow strength far exceeds the measured shear stress unless all deformation is accommodated by dislocation glide in the muscovite.
6) The frictional properties of felsic and mafic samples suggest that deep earthquakes in the East African Rift System are most likely to nucleate in mafic rocks. This means that either the lower crust contains significant volumes of mafic material, or earthquakes nucleate in mafic rocks but are then capable of propagating into surrounding crust.
7) An ideal candidate for lower crustal earthquakes is mafic shear zones in which deformation is localized and strain rates elevated, in rocks that are capable of hosting earthquake slip. Similarly, shear zones with mixed mafic and felsic materials are good candidates if the mafic component is sufficient for earthquake propagation through felsic volumes. We estimate that a critical volume fraction of mafic material is on the order of 80% but acknowledge uncertainties in this calculation which requires more detailed modelling.

Acknowledgements

We like to thank Thony van de Gon-Netscher, Gerard Kuijpers and Floris van Oort for technical support, Johann Diener for discussion, Maartje Hamers for microscope support and Martijn van den Ende for his help in processing data. We also like to thank Marco Scuderi and Changrong He for their excellent reviews and editor Philippe Agard for handling our paper. Financial support from the Dutch Research Council (NWO) through a VIDI grant (nr. 854.12.011 awarded to Niemeijer), from the ERC starting grant SEISMIC (nr. 335915, awarded to Niemeijer), MICA (nr. 715836, awarded to Fagereng) and from EPSRC Global Challenges (PREPARE, grant code EP/P028233/1) is gratefully acknowledged. Mechanical data is available through the EPOS multiscale laboratories data-sharing facility (https://epos-msl.uu.nl/)

References

Albaric, J., Déverchère, J., Petit, C., Perrot, J., & Le Gall, B. (2009). Crustal rheology and depth distribution of earthquakes: insides from the central and southern East African Rift System. Tectonophysics, 468, 28-41.

Albaric, J., Perrot, J., Déverchère, J., Deschamps, A., Le Gall, B., Ferdinand, R.W., Petit, C., Tiberi, C., Sue, C., & Songo, M. (2010). Contrasted seismogenic and rheological behaviours from shallow and deep earthquake sequences in the North Tanzanian Divergence, East Africa. Journal of African Earth Sciences, 58, 799-811.

Beeler, N. M., T. E. Tullis, A. K. Kronenberg, and L. A. Reinen (2007), The instantaneous rate dependence in low temperature laboratory rock friction and rock deformation experiments, Journal of Geophysical Research., 112, B07310, doi:10.1029/2005JB003772.

Blanpied, M., Lockner, D., & Byerlee, J. (1991). Fault stability inferred from granite sliding experiments at hydrothermal conditions. Geophysical Research Letters, 18(4), 609-612. doi:10.1029/91GL00469

Blanpied, M., Lockner, D., & Byerlee, J. (1995). Frictional slip of granite at hydrothermal conditions. Journal of Geophysical Research, 100(B7), 13045-13064.

Blanpied, M., Marone, C., Lockner, D., Byerlee, J., & King, D. (1998). Quantitative measure of the variation in fault rheology due to fluid-rock interactions. Journal of Geophysical Research, 102(B5), 9691 - 9712.

Bloomfield, K. (1966). 1:1,000,000 Geological Map of Malawi. Geological Survey Department: Zomba, Malawi.

Brace, W., & Kohlstedt, D. (1980). Limits on lithospheric stress imposed by laboratory experiments. Journal of Geophysical Research, 85(B11), 6248-6252.

Brodie, K.H. and Rutter, E.H. (1987). Deep crustal extensional faulting in the Ivrea Zone of Northern Italy. Tectonophysics, 140, 193-212.

Carter, G.S., & Bennett, J.D. (1973). The Geology and Mineral Resources of Malawi. Geological Survey Department Bulletin 6, Zomba, Malawi.

Chapola, L.S., & Kaphwiyo, C.E. (1992). The Malawi rift: Geology, tectonics and seismicity. Tectonophysics, 209, 159-164.

Chen, J., & Spiers, C. J. (2016). Rate and state frictional and healing behavior of carbonate fault gouge explained using microphysical model. Journal of Geophysical Research: Solid Earth, 121, 8642–8665. doi:10.1002/2016JB013470

Chester, F. (1995). A rheological model for wet crust applied to strike-slip faults. Journal of Geophysical Research, 100(B7), 13033-13044.

Chester, F., & Higgs, N. (1992). Multimechanism Friction Constitutive Model for Ultrafine Quartz Gouge at Hypocentral Conditions. Journal of Geophysical Research, 97(B2), 1859-1870.

Corti, G., Bonini, M., Conticelli, S., Innocenti, F., Manetti, P. and Sokoutis, D., 2003. Analogue modelling of continental extension: a review focused on the relations between the patterns of deformation and the presence of magma. Earth-Science Reviews, 63(3-4), 169-247.

Craig, T., Jackson, J., Priestley, K., & McKenzie, D. (2011). Earthquake distribution patterns in Africa: their relationship to variations in lithospheric and geological structure, and their rheological implications. Geophysics Journal International, 185, 403-434.

Den Hartog, S., Niemeijer, A., & Spiers, C. (2012). New constraints on megathrust slip stability under subduction zone P-T conditions. Earth and Planetary Science Letters, 353-354, 240-252.

Dieterich, J. (1978). Time-dependent friction and the mechanics of stick-slip. Pure Applied Geophysics, 116, 790-806.

Fagereng, A. (2013). Fault segmentation, deep rift earthquakes and crustal rheology: Insights from the 2009 Karonga sequence and seismicity in the Rukwa-Malawi rift zone. Tectonophysics, 601, 216-225.

Faulkner, D., Sanchez-Roa, C., Boulton, C., & De Hartog, S. (2018). Pore Fluid Pressure Development in Compacting Fault Gouge in Theory, Experiments, and Nature. Journal of Geophysical Research, 123, 226-241. doi:10.1002/2017JB015130

Foster, A., & Jackson, J. A. (1998). Source parameter of large African earthquakes: implications for crustal rheology and regional kinematics. Geophysics Journal International, 134(2), 422-488. doi:https://doi.org/10.1046/j.1365-246x.1998.00568.x

Gu, J., J. R. Rice, A. L. Ruina, and S. T. Tse (1984),Siip motion andstability of a single degree of freedom elastic system with rate and state dependent friction, Journal of the Mechanics and Physics of Solids.. Solids, 32.

Handy, M., & Brun, J. (2004). Seismicity, structure and strength of the continental lithosphere. Earth and Planetary Science Letters, 223(3-4), 427-441. doi:https://doi.org/10.1016/j.epsl.2004.04.021

He, C., T.-f. Wong, and N. M. Beeler, (2003) Scaling of stress drop with recurrence interval and loading velocity for laboratory derived fault strength relations, Journal of Geophysical Research, 108(B1), 2037, doi:10.1029/2002JB001890, 2003

He, C., Luo, L., Hao, Q. M., & Zhou, Y. (2013). Velocity-weakening behavior of plagioclase and pyroxene gouges and stabilizing effect of small amounts of quartz under hydrothermal conditions. Journal of Geophysical Research, 118, 3408-3430. doi:10.1002/jgrb.50280

He, C., Wang, Z., & Yao, W. (2007). Frictional Sliding of gabbro gouge under hydrothermal conditions. Tectonophysics, 445, 353-365.

Ikari, M., Saffer, D., & Marone, C. (2009). Frictional and hydrologic properties of clay-rich fault gouge. Journal of Geophysical Research, 114.

Jackson, J., & Blenkinsop, T. (1993). The Malawi earthquake of March 10, 1989: Deep faulting within the East African rift system. Tectonics, 12(5), 1131-1139.

Jackson, J., & Blenkinsop, T. (1997). The Bilila-Mtakataka fault in Malawi: An active, 100-km long, normal fault segment in thick seismogenic crust. Tectonics, 16(1), 137-150. doi:10.1029/96TC02494

Jackson, J., Austrheim, H., McKenzie, D., & Priestley, K. (2004). Metastability, mechanical strength, and the support of mountain belts. Geology, 32(7), 625-628. doi:10.1130/G20397.1

Kirby, S. (1980). Tectonic stresses in the lithosphere: Constraints provided by the experimental deformation of rocks. Journal of Geophysical Research, 85(B11), 6353-6363. doi:10.1029/JB085iB11p06353

Kirby, S. (1985). Rock mechanics observations pertinent to the rheology of continental lithosphere and the localization of strain along shear zones. Tectonophysics 119, 1-27.

Lavayssière, A., Drooff, C., Ebinger, C., Gallacher, R., Illsley‐Kemp, F., Oliva, S. J., & Keir, D. (2019). Depth extent and kinematics of faulting in the southern Tanganyika rift, Africa. Tectonics, 38, 842‐862.

Lee, H., Muirhead, J.D., Fischer, T.P., Ebinger, C.J., Kattenhorn, S.A., Sharp, Z.D., Kianji, G. (2016). Massive and prolonged deep carbon emissions associated with continental rifting. Nature Geoscience, 9, 145-149.

Luo, Y., Ampuero, J-P. Stability of faults with heterogeneous friction properties and effective normal stress, Tectonophysics, volume 733, 2018, pp. 257-272, doi:10.1016/j.tecto.2017.11.006

Mackwell, S., Zimmerman, M., & Kohlstedt, D. (1998). High-temperature deformation of dry diabase with application to tectonics on Venus. Journal of Geophysical Research, 103(B1), 975-984. doi:10.1029/97JB02671

Mariani, E., Brodie, K.H. and E.H. Rutter (2006) Experimental deformation of muscovite shear zones at high temperatures under hydrothermal conditions and the strength of phyllosilicate-bearing faults in nature, Journal of Structural Geology 28, 1569-1587, doi:10.1016/j.jsg.2006.06.009

Marone, C. (1998). Laboratory-derived friction laws and their applications to seismic faulting. Annu. Rev. Earth Planet. Sci., 26, 643-696.

Menegon, L., Pennacchioni, G., Malaspina, N., Harris, K. and Wood, E. (2017). Earthquakes as precursors of ductile shear zones in the dry and strong lower crust. Geochemistry, Geophysics, Geosystems 18, 4356-4374.

Miller, S.A., Collettini, C., Chiaraluce, L., Cocco, M., Barchi, M., & Kaus, B.J.P. (2004). Aftershocks driven by a high-pressure CO_2 source at depth. Nature, 427, 724-727.

Niemeijer, A., Spiers, C., & Peach, C. (2008). Frictional behavior of simulated quartz fault gouges under hydrothermal conditions: Results from ultra-high strain rotary shear experiments. Tectonophysics, 460, 288-303.

Niemeijer, A. R., Boulton, C., Toy, V. G., Townend, J., & Sutherland, R. (2016). Large-displacement, hydrothermal frictional properties of DFDP-1 fault rocks, Alpine Fault, New Zealand: Implications for deep rupture propagation. Journal of Geophysical Research, 121, 624–647. doi:10.1002/2015JB012593

Nyblade, A., & Langston, C. (1995). East African earthquakes below 20 km depth and their implications for crustal structure. Geophysical Journal International, 121, 49-62.

Parry, W.T. & Bruhn, R.L. (1990). Fluid pressure transients on seismogenic normal faults. Tectonophysics, 179, 335-344.

Ranalli, G.,1995. Rheology of the Earth , 2nd edition.Chapman&Hall,London

Reinen, L., & Weeks, J. (1993). Determination of Rock Friction Constitutive Parameters Using an Iterative Least Squares Inversion Method. Journal of Geophysical Research, 98(B9), 15,937 - 15,950.

Ruina, A. (1983). Slip instability and state variable friction laws. Journal of geophysical research, 88, 10359-10370.

Scholz, C. (1988). The brittle-plastic transition and the depth of seismic faulting. Geologische Rundschau, 77/1, 319-328.

Scholz, C. (1998). Earthquakes and friction laws. Nature, 391, 37-42.

Scholz, C. (2002). The mechanics of earthquakes and faulting. Cambridge University Press.

Shea,W.T., Kronenberg, A.K., 1992. Rheology and deformation mechanisms of an isotropic mica schist. Journal of Geophysical Research 97, 15201-15237.

Shimamoto, T. (1986), Transition between frictional slip and ductile flow for halite shear zones at room temperature, Science, 231(4739), 711–714.

Shudofsky, G., Cloetingh, S., Stein, S., & Wortel, R. (1987). Unusually deep earthquakes in East Africa: Constraints on the thermo-mechanical structure of a continental rift system. Geophysical Research Letters, 14(7), 741-744.

Sibson, R.H. (1980). Transient discontinuities in ductile shear zones. Journal of Structural Geology 2, 165-171.

Skarbek, R. M., A. W. Rempel, andD. A. Schmidt (2012), Geologic heterogeneity can produce aseismic slip transients, Geophysical Research Letters, 39, L21306, doi:10.1029/2012GL053762.

Tullis, J. and R.A. Yund (1977). Experimental deformation of dry Westerly Granite. Journal of Geophysical Research, vol. 82, no. 36, 5705-5718.

Verberne, B., Niemeijer, A., De Bresser, J., & Spiers, C. (2015). Mechanical behavior and microstructure of simulated calcite fault gouge sheared at 20-600C: Implications for natural faults in limestones. Journal of Geophysical Research, 120, 8169-8196. doi:10.1002/2015JB012292

Verberne, B.A., Chen, J., Niemeijer, A.R., de Bresser, J.H.P., Pennock, G.M., Drury, M.R. and C.J. Spiers (2017) Microscale cavitation as a mechanism for nucleating earthquakes at the base of the seismogenic zone. Nature communications, 8:1645, doi: 10.1038/s41467-017-01843-3

Versfelt, J. and Rosendahl, B.R. (1989). Relationship between pre-rift structures and rift architecture in Lakes Tanganyika and Malawi, East Africa. Nature 337, 354-357.

White, S.H., & Knipe, R.J. (1978). Transformation and reaction-enhanced ductility in rocks. Journal of the Geological Society of London, 135, 513-516.

Wintsch, R.P., Chrisstofferson, R., & Kronenberg, A.K. (1995). Fluid-rock reaction weakening of fault zones. Journal of Geophysical Research, 100, 13,021-13,032.

Yang, Z., & Chen, W. (2010). Earthquakes along the East African Rift System: A multiscale, system-wide perspective. Journal of Geophysical Research, 115, B12309.